Geoscience Frontiers 15 (2024) 101724

Contents lists available at ScienceDirect

Geoscience Frontiers

journal homepage: www.elsevier.com/locate/gsf

Research Paper

Vanadium mineralization at Los Chihuidos sediment-hosted Cu–V deposit, Neuquén Basin, Argentina: An approach to vanadium ore forming processes

Ana L. Rainoldi [a,b,*], Daniel Beaufort [c], Marta B. Franchini [b,d], Adolfo Giusiano [e], Sabine Petit [c], Patricia Patrier [c], M. Josefina Pons [b,f]

[a] Dpto. de Geología, Universidad Nacional del Sur (UNS), 8000 Bahía Blanca, Argentina
[b] Consejo Nacional de Investigaciones Científicas y Técnicas, Centro Patagónico de Estudios Metalogenéticos, Argentina
[c] Université de Poitiers, IC2MP, CNRS-UMR 7285, Hydrasa, F-86022 Poitiers Cedex, France
[d] Universidad Nacional del Comahue, Facultad de Ingeniería, Departamento de Geología y Petróleo, 8300 Neuquén, Argentina
[e] Consultant Geologist, 8300 Neuquén, Argentina
[f] Universidad Nacional de Río Negro, Instituto de Investigación en Paleobiología y Geología, Río Negro, Argentina

ARTICLE INFO

Article history:
Received 25 April 2023
Revised 17 August 2023
Accepted 2 October 2023
Available online 10 October 2023
Handling Editor: C. Manikyamba

Keywords:
Clay minerals
V-chlorite
Redox front
Bleaching
Hydrocarbons

ABSTRACT

Vanadium mineralization at Los Chihuidos deposit of the Neuquén Basin is linked to the development of a redox front system related to the inflow of hydrocarbons into the red sandstone of the Huincul Formation. Interaction of hydrocarbons with oxidized red beds and connate water generated redox reactions where hematite was dissolved due to iron reduction resulting in the discoloration of the red strata. At the contact between oxidized red sandstone and reduced white sandstone, precipitation of specific mineral phases resulted in the V ore with minor amounts of Cu. With the implementation of the redox interface, abundant V-montmorillonite and V-hematite precipitated at the more oxidizing conditions and Cu-V-corrensite-type at the more reducing conditions of the redox front. As the redox front advanced with fluids constantly migrating into the reservoir, more reducing conditions were stablished, promoting chloritization and minor illitization with V-Cu incorporation and continuous upgrading of the ore. Main ore mineralogy consists of clay minerals including V-bearing montmorillonite, Cu-V-corrensite-type, V-di-trioctahedral chlorite and Cu-tri-trioctahedral chlorite with minor V-illite–smectite mixed-layer minerals and associated secondary V-hematite. Chloritization over illitization was favored due to high amounts of Fe and Mg in detrital clasts and in connate fluids and by low K availability related to low amounts of detrital K-feldspar. The spatial transition of V and /or Cu bearing clay minerals observed through the mineralized redox front at Los Chihuidos deposit (kaolinite → smectite → illite/smectite → corrensite-type → di- trioctahedral -chlorite → tri- trioctahedral -chlorite) and the related variation of V–Cu concentrations in bulk rock are indicative of increasing pH and decreasing Eh of resident solutions from red to white sandstones during the hypogene mineralization process. Late influx of Cu-rich oxidized basinal brines precipitated main copper ore with Cu-sulfides in the white sandstone up to the contact with the redox front in contact with hydrocarbons. During uplift and exhumation, percolation of meteoric water promoted remobilization of V and Cu and the precipitation of oxidized V–Cu ore.

© 2023 China University of Geosciences (Beijing) and Peking University. Published by Elsevier B.V. on behalf of China University of Geosciences (Beijing). This is an open access article under the CC BY-NC-ND license (http://creativecommons.org/licenses/by-nc-nd/4.0/).

1. Introduction

The Neuquén Basin of central western Argentina hosts several sediment-hosted stratiform Cu (SSC) deposits with minor V, U, and Ag (Pons et al., 2009, 2014; Zientek et al., 2015; Paz et al., 2016; Rainoldi et al., 2019) and Zn–Pb occurrences (Pons et al., 2021) which represent the main metalliferous resource of the region. The Los Chihuidos SSC deposit (37°50′30″S, 69°27′W) is located in the central part of the Neuquén Basin, near the Sierra Chata and Aguada Pichana gas reservoirs, and it is hosted in the Huincul Formation (Late Cenomanian–Early Turonian) of the Neuquén Group. With inferred resource of 151 Mt @ 0.3% Cu and V as

* Corresponding author at: Dpto. de Geología, Universidad Nacional del Sur (UNS), 8000 Bahía Blanca, Argentina.
E-mail addresses: analaura.rainoldi@uns.edu.ar, analaurarl@hotmail.com (A.L. Rainoldi).

https://doi.org/10.1016/j.gsf.2023.101724
1674-9871/© 2023 China University of Geosciences (Beijing) and Peking University. Published by Elsevier B.V. on behalf of China University of Geosciences (Beijing). This is an open access article under the CC BY-NC-ND license (http://creativecommons.org/licenses/by-nc-nd/4.0/).

the main by-product (average grade of 0.1% V; Orión del Sur 2008, 2012), Los Chihuidos represents the highest V accumulation in the region.

Red sandstone, siltstone and conglomerate of the Huincul Formation at the site of mineralization are bleached and strongly impregnated with bitumen, which is absent in the unaltered rocks (Rainoldi et al., 2014, 2019). The reaction of hydrocarbons with the red beds and formation water resulted in a redox system with characteristic color zoning, defined by diagenetic facies (Beitler et al., 2005), according to their changing redox conditions. The white beds represent the reduced compartment, the red beds the oxidized compartment, and the gray and brown sandstones the redox front (Rainoldi et al., 2014, 2019). The mineralized redox system has been also described southward of the study area (Testi and Giusiano, 2020), evidencing its development at regional scale. Rainoldi et al. (2019) proposed a genetic model for the Los Chihuidos deposit which involves two steps of fluid flow related to the reactivation of brittle faults during the Tertiary Andean tectonism: (i) bleaching of red beds by reaction with hydrocarbon-bearing fluids and V mineralization and (ii) precipitation of Cu sulfides by reduction of oxidized metal-rich basinal brines in the hydrocarbon Huincul reservoir. This model emphasis mainly the characteristics and genesis of the Cu mineralization.

Vanadium is a strategic metal used principally in the production of metal alloys. The emerging new industries related to clean energies like wind, solar, and other renewable, with intermittent power sources, requires a large-scale electricity storage capacity like vanadium redox-flow batteries. Other use of vanadium is in lithium-vanadium-phosphate batteries for electric cars. This scenario provides a major potential future use of vanadium. Vanadium deposits are globally distributed with the majority of V production (in 2012) being from China (37%), South Africa (35%), and Russia (25%) (Kelley et al., 2017). Small deposits in Argentina are unlikely to be economically significant resources, then, the need for new deposits discovery remains critical for the country. Vanadium is extracted from different mineral deposits and even from fossil fuels. Major vanadium accumulations occur in vanadiniferous titanomagnetite deposits, which consist of magmatic ilmenite and magnetite containing 0.2–1 wt.% V_2O_5 (Kelley et al., 2017). However, sedimentary-hosted V deposits offer a potential alternative where important sources of V have been related to clay minerals, mainly chlorite in sandstone-hosted deposits (Whitney and Northrop, 1986; Northrop et al., 1990; Hansley and Spirakis 1992; Meunier, 1994; Schmid et al., 2020) and illite, smectite and mixed-layer minerals in shale-hosted deposits (McKelvey et al. 1986; Lewis et al., 2010; Peacor et al., 2000). In the case of chlorite, its internal structure allows substantial amounts of substitutions, resulting in exotic chlorites with high amounts of chromium, nickel, lithium or vanadium (Whitney and Northrop, 1986; Meunier, 1994).

This contribution presents the first mineralogical and geochemical study of the vanadium-rich zones at Los Chihuidos deposit. The manuscript aims to give the distribution and characterization of the V ore and discuss the plausible sources of V and mechanisms for its precipitation. Previous studies have shown that during organic matter diagenesis, V becomes associated with clay minerals and oxides (e.g., Hansley and Spirakis, 1992). In this study we show that the interaction of hydrocarbons with oxidized red beds may result in diagenetic processes where V becomes associated with clay minerals and oxides, always localized at the redox front with fluctuating Eh–pH conditions. The model proposed has important implications for understanding the formation of V mineralization in the SSC deposits of the Neuquén Basin, which has close similarities with sediment hosted V mineralization worldwide, including the very well-known uranium-vanadium deposits from the Colorado Plateau (Whitney and Northrop, 1986; Meunier, 1994). The presence of a regional-scale alteration halo related to the formation of the redox system and the V mineralization suggests a significant sedimentary sink for this element.

2. Geological background

2.1. Regional geology

The Neuquén Basin is a retroarc foreland basin located in west-central Argentina (Fig. 1a). The tectonic evolution of this basin began in the Late Triassic and Early Jurassic driven by extensional collapse of the Permian-Triassic orogenic belt, followed by several episodes of structural inversion (Vergani et al., 1995). The Neuquén Basin records at least 220 Ma of basin subsidence with 7000 m thick Upper Triassic–Cenozoic preserved basin infill of marine, evaporite, and continental sedimentary and volcaniclastic rocks (Fig. 1b). This geological evolution resulted in a stratigraphic record of the basin characterized by the development of several source and reservoir hydrocarbon rocks.

The first episode of sedimentation in the Neuquén Basin is represented by volcanic, volcaniclastic, and associated clastic rocks of the Precuyo Group deposited in isolated half-grabens. From the Early Jurassic to the Middle Cretaceous, sedimentary rocks of the Cuyo, Lotena, Mendoza, and Bajada del Agrio groups were deposited during successive transgressions from the Pacific Ocean prior to the Andean Cordillera uplift (Mosquera and Ramos, 2006). The Pliensbachian–Callovian Cuyo Group includes deep-marine organic-rich shale, shallow-marine to deltaic sandstone, and evaporite deposits. The Callovian–Oxfordian Lotena Group was deposited during the tectonic inversion of the basin (Vergani et al., 1995). It consists of deltaic to shallow-marine clastic deposits and marine limestone, finishing with thick evaporite deposits. The Kimmeridgian–Barremian Mendoza Group begins with eolian-fluvial and lacustrine sandstone followed by deep-marine organic-rich shale, nearshore limestone and continental to shallow-marine deposits and ends up with deep marine organic-rich shale interbedded with eolian sandstone. The Barremian-Albian Bajada del Agrio Group comprises evaporitic and clastic deposits, representing the last connection with the Pacific Ocean. Cenomanian is characterized by the deposition of 1300 m of synorogenic fluvial, lacustrine and eolian red beds from the Neuquén Group (Cazau and Uliana, 1973) (Fig. 1b). In the Maastrichtian, the first Atlantic transgression occur in the region with the deposition of shallow-marine sandstone, siltstone, and fossiliferous limestone from the Malargüe Group. Tertiary is characterized by the deposition of synorogenic siliciclastic deposits and associated volcanism.

Tectonic activity and deformation in the Neuquén Basin varied in intensity and location, resulting in a complex mosaic of modern morphostructural units: Andean fold and thrust belt, Agrio fold and thrust belt, Loncopué Trough, Huincul High, Los Chihuidos High, Embayment, and Outer Shelf (Fig. 1a). The study area is located in the Los Chihuidos High, which represents a basement cored asymmetric anticline 70 km long characterized by a sharp western forelimb and a gently extended eastern back limb, overlaid by a series of secondary folds developed along its axis (Mosquera and Ramos, 2006). No major faults affect the structure, but regional lineaments and related fractures with NW–SE, NE–SW and W–E orientations have been identified (Fig. 2). Its uplift has been explained as tectonic inversion of Triassic half-grabens (Precuyo Group) in a foreland basin during the Jurassic to Early Cretaceous (Maretto and Pángaro, 2005; Mosquera and Ramos, 2006). Late Cretaceous tectonism was characterized by a reactivation pulse with the Agrio fold and thrust belt configuration westward, which caused a low-angle unconformity (inter-Cenomanian) at the top of

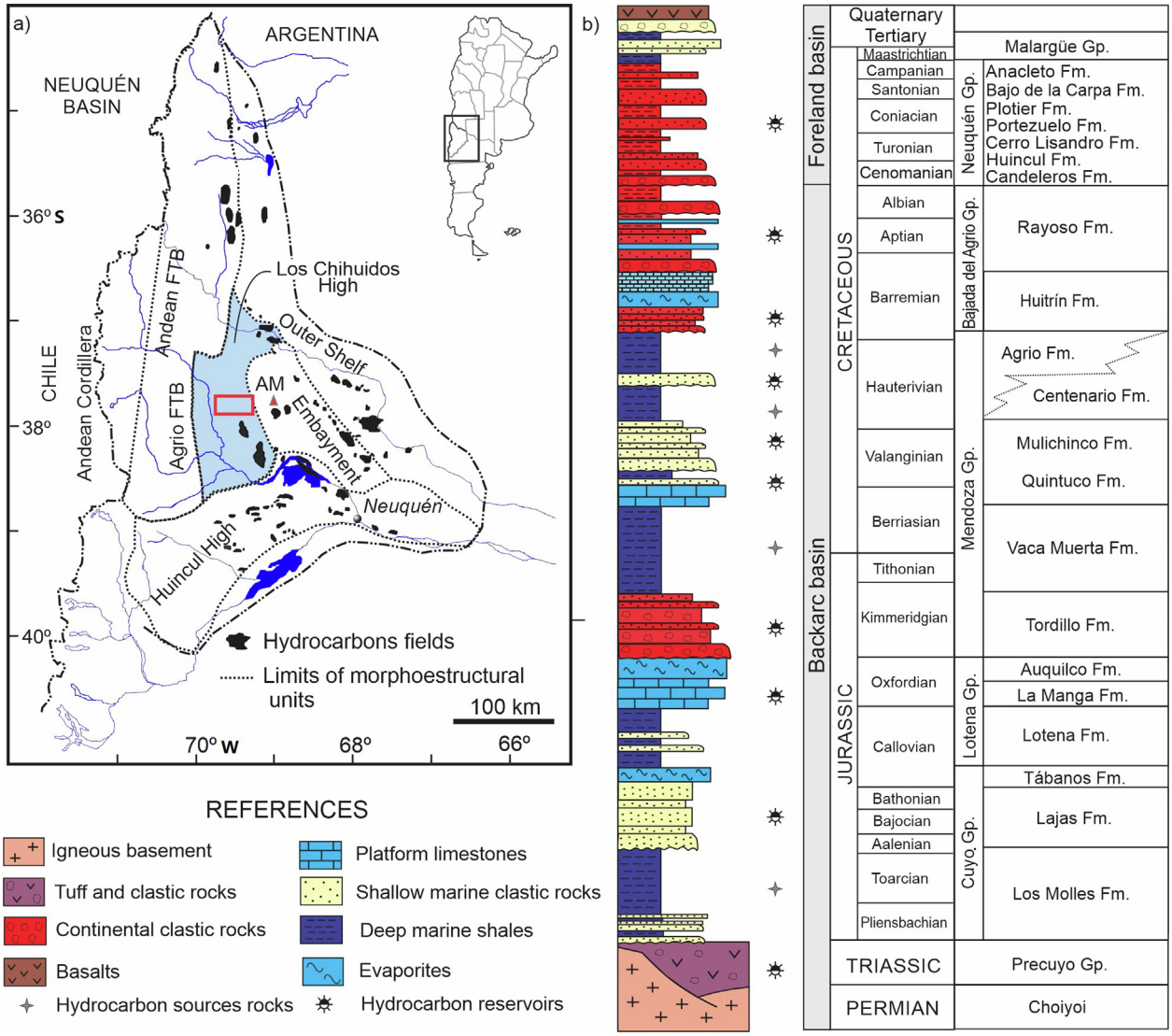


Fig. 1. Geologic setting of the Neuquén Basin. (a) Map of the Neuquén Basin, Argentina, showing the main morphostructural units and the location of the study area Los Chihuidos deposit (red rectangle) (modified form Giusiano and Bouhier, 2009). (b) Chronostratigraphic column of the Neuquén Basin (after Zavala et al., 2008). AM: Auca Mahuida volcano; FTB: Fold Thrust and Belt. (For interpretation of the references to color in this figure legend, the reader is referred to the web version of this article.)

the Rayoso Formation and the deposition of synorogenic deposits (Neuquén Group; Cazau and Uliana, 1973) (Fig. 1b). During the Tertiary, tectonic inversion took place resulting in the final configuration of the Los Chihuidos High (Zamora Valcarce et al., 2009).

2.2. Local geology

The Los Chihuidos deposit is located in the western limb of the Los Chihuidos High structure (Fig. 1a). The Los Chihuidos High has been described as a tectonic inversion of Triassic half grabens in a foreland basin (Maretto and Pángaro 2005), and the last compressive episodes occurred during Tertiary (Mosquera and Ramos 2006). Apatite fission-track dating identified three cooling and uplift events: one through Maastrichtian-Eocene (70–50 Ma) with the erosion of 1000 m of sedimentary deposits and other two during Miocene at 20–25 Ma and 14 Ma with the erosion of 700 m and 750 m of sediments, respectively (Zamora Valcarce et al., 2009).

Southward of the study area, several gas fields produce hydrocarbons from the Mulichinco Formation (Aguada Pichana and Sierra Chata gas fields; Anechine et al., 2002; Vottero and González, 2002). In the Los Chihuidos deposit gas chimneys have been identified in seismic lines (Cevallos et al., 2014). These gas chimneys connect the deepest gas kitchen of the Los Molles Formation with the reservoirs (Mulichinco Formation) and source rocks (Vaca Muerta Formation) of the Mendoza Group, and with the Upper Cretaceous Neuquén Group (Cevallos et al., 2014).

The continental sedimentary succession gently dips 2°–5° to the east and includes the Rayoso Formation from the Bajada del Agrio Group (Barremian–Albian) and the Candeleros, Huincul, Cerro Lisandro, Portezuelo, Plottier and Bajo de la Carpa formations from the Neuquén Group (Cenomanian–Campanian) (Fig. 1b, 2). The Candeleros Formation, which consists of fluvial deposits associated with paleosols and swamps deposits, is separated by the underlying fluvial deposits of the Rayoso Formation by a regional inter-Cenomanian unconformity. It is overlaid by the fluvial sandstones of the Huincul Formation and with the fluvial, eolian and lacustrine deposits of Cerro Lisandro, Portezuelo, Plottier and Bajo de la Carpa formations to the east. Subvolcanic Tertiary dikes of the Desfiladero Formation (Ramos and Barbieri, 1989) were emplaced in extensional zones transversal to the main axis folds (Ardolino and Franchi, 1996). Parva Negra small, intraplate, alkali-basalt cones (Pliocene, 4.5 Ma; Ramos and Barbieri, 1989) and the Auca

Mahuida monogenic volcano (Pleistocene–Holocene, 1.78–1.38 Ma; Kay et al., 2004) complete the stratigraphic succession (Fig. 2).

The Huincul Formation hosts copper and vanadium mineralization. It consists of very coarse/coarse- to medium-grained, medium- to well-sorted and texturally immature feldspathic litharenite (Folk et al., 1970) with subordinate siltstone and sparse intra-formational conglomerate with locally abundant pieces of fossil woods. This succession was deposited in meandering rivers governed by a complex balance between subsidence and sediment supply related to the westward growth of the Andean Cordillera (Garrido, 2010; Rainoldi et al., 2012). Fabric is grain-supported and packing is dominantly loose, with mostly tangential intergranular contacts. The detrital mineralogy has little regional variation and typically includes rock fragments, mono- and polycrystalline quartz, and feldspar with plagioclase ≫ potassic feldspar and accessory martite (i.e., hematite pseudomorph after magnetite), micas, tourmaline, zircon, and rutile. The most common rock fragments are a great variety of volcanic types with predominance of basic-mesosilicic and minor felsitic-vitric compositions with subordinated plutonic, sedimentary, and metamorphic grains (Rainoldi et al., 2014). Basic volcanic fragments commonly present lathwork grains with plagioclase laths in intersertal texture whereas mesosilicic volcanic fragments are characterized by microlitic grains with euhedral plagioclase plates in pilotaxic textures; both lathwork and microlitic grains are partially altered to chlorite. Felsitic and vitric rock fragments are characterized by microcrystalline mosaic of quartz and feldspar and vitrophiric grains; felsitic and vitric rock fragments as well as detrital feldspars are partially altered to illite. Plutonic fragments correspond to the quartz-feldspathic granitic-type and metamorphic grains include chloritized schists. Mud intraclasts are locally important, mainly located at the base of the fluvial paleochannels; mud intraclasts as some volcanic and volcaniclastic grains are frequently compacted to pseudomatrix. Sediments were mainly supplied by the erosion of Jurassic-Cretaceous volcanic arc rocks which were sourced near the orogenic front (Di Giulio et al., 2012), explaining the high number of volcanic fragments, mainly basalts and andesites. Detrital grains of feldspar and quartz derived from plutonic and metamorphic rocks sourced from the basement (Di Giulio et al., 2012) and from the growing of the fold thrust and belt between the volcanic arc and the Neuquén Basin. Syndepositional Permian, Triassic, and Jurassic zircons suggest that the Huincul Formation was fed from the western Cordillera, with detrital grains sourced by the volcanic arc and by the fold thrust and belt, and with contribution of material supplied from the basement located in the foreland (Tunik et al., 2008; Di Giulio et al., 2012).

3. Alteration and copper mineralization of the huincul formation

At a regional scale, the mineralization occurs within a large alteration halo that has been described by Rainoldi et al. (2014). This halo forms a north–south front of 30 km long and 12 km wide of bleached beds that alternate with red beds (Figs. 2, 3a) and spreads outwards the deposit area reaching a maximum extension of 100 km (Testi and Giusiano, 2020). The alteration is mostly developed in the coarse-grained sandstone. The transition from

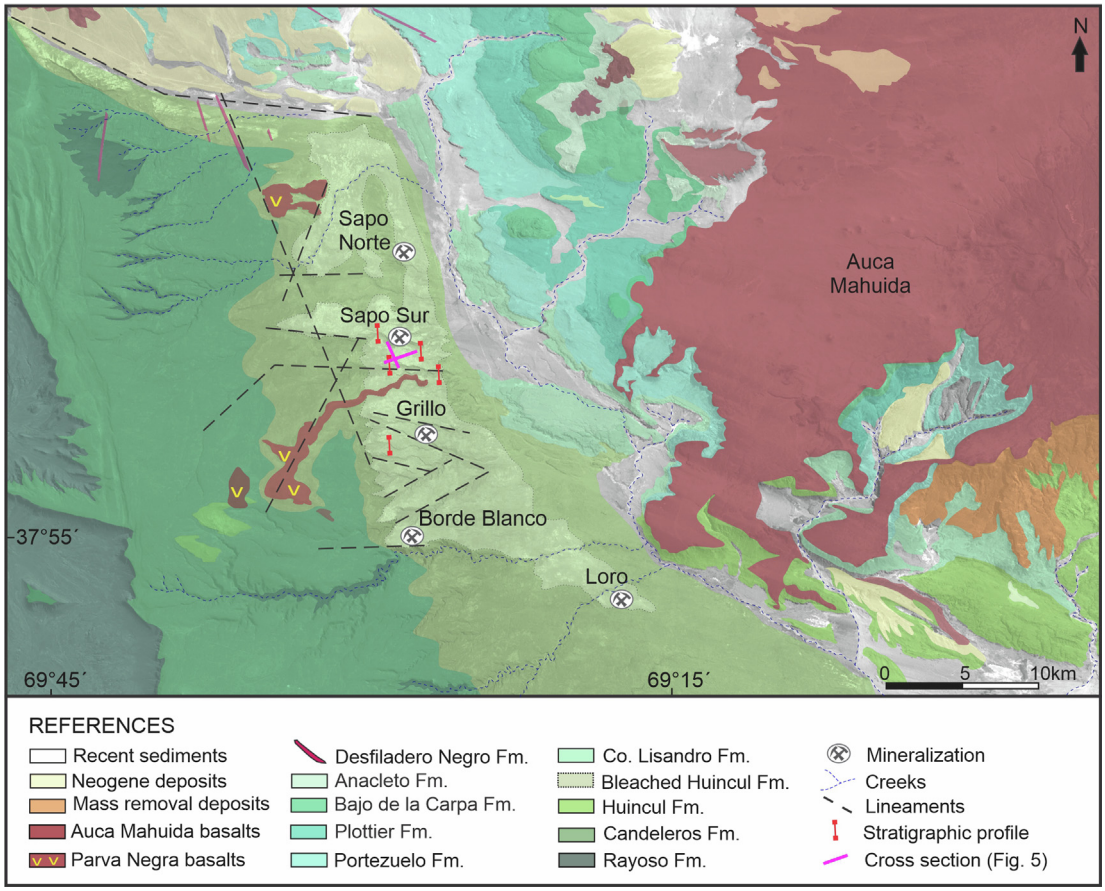


Fig. 2. Geological map of the Los Chiuidos deposit (modified from Leanza et al., 2011).

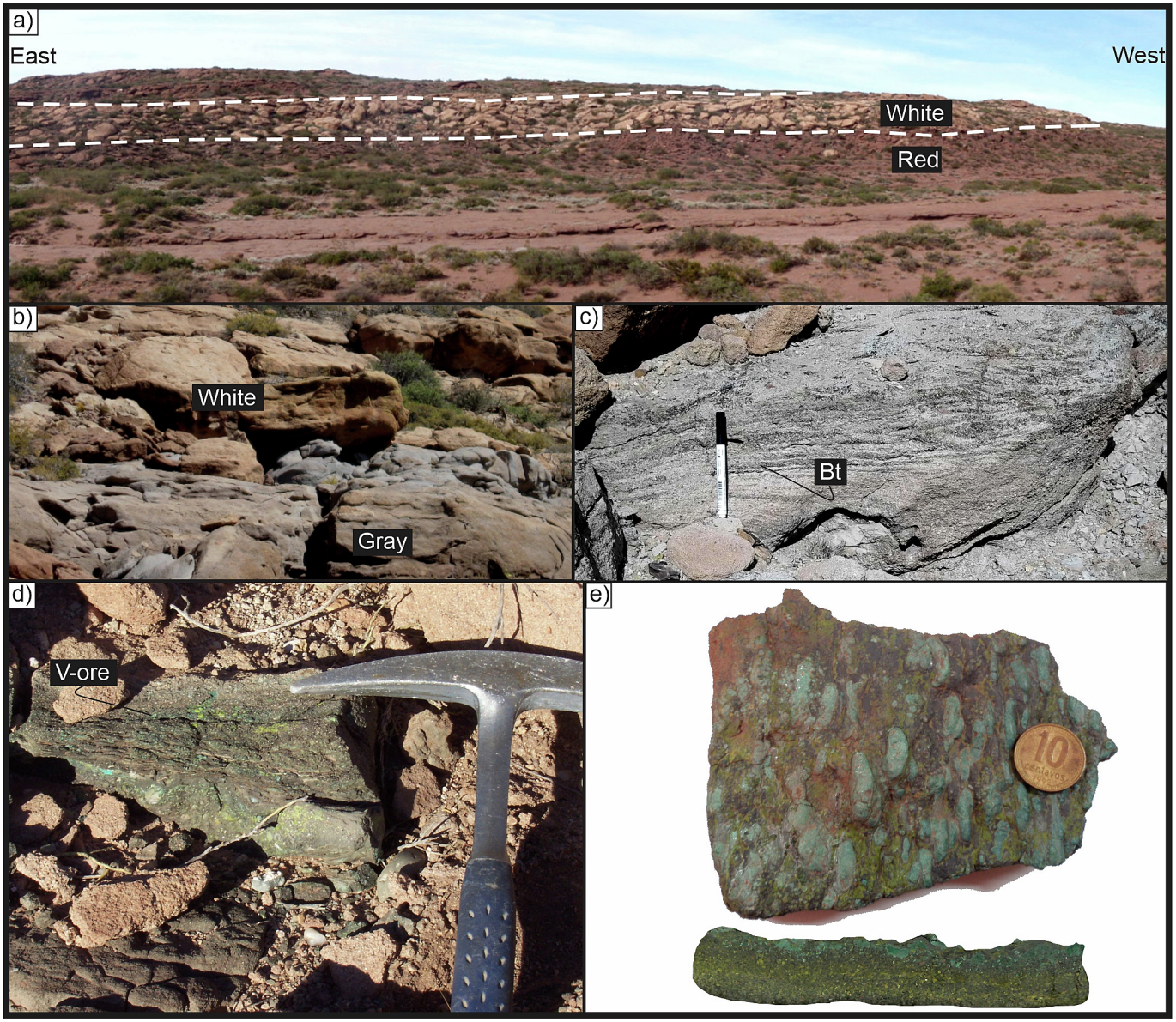


Fig. 3. Photographs from outcrops showing the main characteristics of the vanadium host rock and mineralization. **(a)** Bleached (white) sandstone interbedded into the red bed sequence. **(b)** Gray sandstone developed at the contact with the white sandstone. **(c)** Bitumen impregnations following bedding planes in altered bleached sandstone. **(d)** Vanadium mineralization in dark greenish gray sandstone. **(e)** Tree bark mold mineralized with supergene oxidized vanadium (yellow color) and copper (light blue color) minerals. *Bt: bitumen.* (For interpretation of the references to color in this figure legend, the reader is referred to the web version of this article.)

red to bleached zones is either crosscutting across stratigraphic boundaries or following sedimentary beds; gray and/or brown sandstones occur at the contact between the formers (Fig. 3b). Discoloration of the more permeable interconnected beds suggests that host-rock porosity and permeability played a key role on the bleaching progress. Clasts, authigenic clays, and pores are impregnated with bitumen. The degree of impregnation could be variable, disseminated in scarce specks to highly concentrated in preferential bedding planes (Fig. 3c) and pipes structures, which represented potential zones of high paleo-permeability.

In the study area, unaltered red beds and altered white, gray and brown sandstones have the same modal composition, therefore, they differ in their diagenetic minerals being mentioned as diagenetic facies (Beitler et al., 2005; Rainoldi et al., 2014). Red beds are characterized by the presence of hematite coatings, kaolinite, quartz and albite overgrowths, patches of turbid calcite and minor baryte. The white sandstone is free of hematite, shows a noticeable increase of the secondary porosity and new authigenic minerals including smectite, pyrite, and limpid poikilotopic calcite. The gray sandstone contains abundant smectite ± chlorite-smectite mixed-layers and secondary V-bearing hematite. When chlorite/smectite predominates, the rocks turn to tan hue defining the brown sandstone (Rainoldi et al., 2014). Copper mineralization occurs in the white sandstone (Fig. 3a) in contact with bitumen impregnations and vegetable fragments and consists of chalcocite-djurleite replaced by supergene chrysocolla >malachite > covellite > brochantite > azurite > cuprite with traces of very fine-grained pyrite and calcite as gangue minerals. Copper minerals are distributed along bedding planes and in fractures and pipes with NW–SE and NE–SW orientations. Other occurrences include tree bark molds and at the contact between sandstone and silicified woods with the same NNW orientation as paleochannels and mineralization occurring after silicification. The vanadium mineralization (Fig. 3d, e) is as by-product of the copper ore.

4. Materials and methods

Outcrops were studied in the Los Chihuidos SSC deposit in well-exposed canyons where five stratigraphic profiles have been done and compared with previous profiles from the area (Rainoldi et al., 2014). Representative samples from the selected profiles were collected for laboratory analysis. Samples collected (n = 52) were analyzed first with a binocular polarizing microscope under transmitted and reflected light for the petrographic characterization. The clay minerals were identified using a Bruker D8 Advance X-ray diffractometer equipped with a linxeye detector. Due to the poorly consolidated state of the samples, sandstones were gently disaggregated in water and the clay fraction put in suspension by ultrasonic treatment. Clay size fractions <4 μm were extracted by sedimentation for oriented powder mounts. No cation exchange was performed. Diffracted beam CuKα_{1+2} radiation was used (40 kV, 40 mA). Relative humidity was not controlled during data acquisition. Less than 2 μm clay size fractions from representative samples were extracted by sedimentation and treated with calcium saturation to permit a better identification of the type of swelling mixed-layer minerals present in the sample. A part of the clay fraction of the selected samples was prepared for randomly oriented powder mounts in order to determine the (060) spacing which is diagnostic for recognition of the di-, di-tri or tri-octahedral minerals.

Representative samples were selected for scanning electron microscope (SEM) observations, which were made on small freshly fractured bulk rock samples and on polished thin sections that were previously coated with carbon. Chemical composition, morphology, and texture of clay mineral assemblage were studied using a JEOL®5600 electron microscope equipped with a Bruker energy dispersive X-ray spectroscopy detector (EDX). Analytical conditions were as follows: accelerating voltage 15 kV, probe current 1nA, working distance 17 mm, counting time of 100 s. The analyzed elements were Na, Mg, Al, Si, Mn, Fe, Ti, K, Ca and Cu. SEM/EDX is appropriate for the quantitative chemical analysis of clay particles because the very small electron-matter interaction volume (a few μm^3) strongly limits the risk of chemical contamination by mineral impurities. Moreover, SEM/EDX permits analysis of all the chemical elements of interest simultaneously. For quantitative EDX analyses the microanalysis system was calibrated using synthetic and natural oxides and silicates standards ($MnTiO_3$, hematite, albite, orthoclase, and diopside) and corrections were made using a ZAF program. The relative errors on the analyzed values are < 1.5% (except Na which is 3%). Total Fe has been arbitrarily considered as Fe^{2+} or Fe^{3+} according to the nature of the analyzed mineral.

Mid Infrared (MIR) spectra (400–4000 cm^{-1}) of clay material were acquired on KBr pellets using a Nicolet 760 FTIR (Fourier Transformation Infrared Spectroscopy) spectrometer equipped with a Potassium Bromide (KBr) beam splitter and DTGS-KBr detector. The resolution was set at 4 cm^{-1} with co-addition of 100 scans. KBr pellets contained 1 mg of sample for 150 mg of KBr powder, crushed into a mortar and pressed under 8 tons for 5 min in hydraulic press before drying at 120 °C.

A group of samples (n = 19) were analyzed for major, trace, and rare earth elements by inductively coupled plasma-emission spectrometry (ICP-ES) and ICP-mass spectrometry (ICP-MS), titration for FeO and coulometry for CO_2, at Actlabs Laboratory (Activation Laboratories LTD) in Ontario, Canada (Tables 1 and 4). Metal assays of cuttings were performed by Alex Stewart Laboratory (Assayers) Argentina S.A. at intervals of 1 m (Orión del Sur 2008, 2012) and have been used for the construction of geochemical cross sections.

5. Results

5.1. Vanadium ore

Vanadium ore is located in the Huincul Formation at the base of the NNW fluvial paleochannels and towards the contact with flood plain deposits (Figs. 4 and 5a). Fluids were channeled through the paleochannels which comprise the coarsest-grained facies but also affected the finer-grained facies of the flood plain deposits located at the base. The V horizons deepen to the east, following the Los Chihuidos anticline structure (Figs. 4 and 5b). The main orebody is located in the gray sandstone defined by Rainoldi et al. (2014, 2019) occurring between the red and white sandstones. Isolated sectors with high V grades have been identified towards the contact with the white sandstone, where the rock turns to dark greenish gray in color (Figs. 3d, 4). Although major V mineralization is concordant or peneconcordant with the stratification, minor discordant mineralization occurs in fractures, pipes and tree bark molds (Fig. 3e). Vanadium mineralization is mostly concentrated in hypogene clay minerals and in supergene oxides, vanadates and urovanadates (Fig. 3d, e).

Vanadium contents and distribution are highly variable. In outcrops, the orebody is relatively thin, with thickness up to 9 m and V concentrations between 263 ppm and 1840 ppm (Fig. 4, Table 1) with an average content of 890 ppm, that is considerably higher than those of typical sandstone (20 ppm; Turkekian and Wedepohl, 1961). Sandstones with Cu-mineralization have V anomalies from 102 ppm to 641 ppm, but when oxidized ore predominates, V reaches values as high as 2516 ppm (Table 1). At depth, the V orebody is much better developed, reaching concentrations higher than 1% V in ~20 m-thick sandstone horizons (Orión del Sur SA, 2012). In some cases, high values of V occur at the bottom of drillholes, with the possibility of increasing ore grades and thicknesses with depth. Similar V concentrations, variable between 0.1% and 1.5%, have been determined in the Campesino U-V deposit located 50 km south of the study area (Testi and Giusiano, 2020). These values are comparable and even higher than V contents in other vanadium sandstone deposits (average 3004 ppm; Northrop et al., 1990) and vanadium shale deposits (220–7390 ppm; Lewis et al., 2010).

5.2. Vanadium clay minerals distribution in a redox system

Different compartments of the redox system are characterized by their coloration which is correlated not only with the distribution of hematite, but also with authigenic minerals, especially clay minerals associations and metal (V-Cu) content (Fig. 6). The regionally oxidized red beds contain hematite coatings, kaolinite fills pore spaces and lacks V. In the altered white, gray, brown and dark greenish gray sandstones, a complex suite of secondary clay minerals replaces kaolinite, detrital Al-bearing silicates and fills the porosity. In the reduced white beds, kaolinite is partially replaced by smectite with traces of V (Fig. 7a), which could also fill the pore spaces in contact with previous feldspar and quartz overgrowths; traces of anatase have been also observed (Fig. 7b). At the redox front, where hypogene V ore occurs, increases the amount and complexity of clay minerals. From the red towards the white sandstones a clay mineral transition is recorded from smectite ± illite–smectite to chlorite-smectite mixed-layer minerals (corrensite-type) and finally to chlorite. The increases of chloritization correlates with the increases of the V content (Fig. 6). In the gray beds, which represent the most widespread and oxidizing portion of the redox front, abundant V-bearing smectite fills the pore spaces and replaces previous kaolinite (Fig. 7c) accompanied

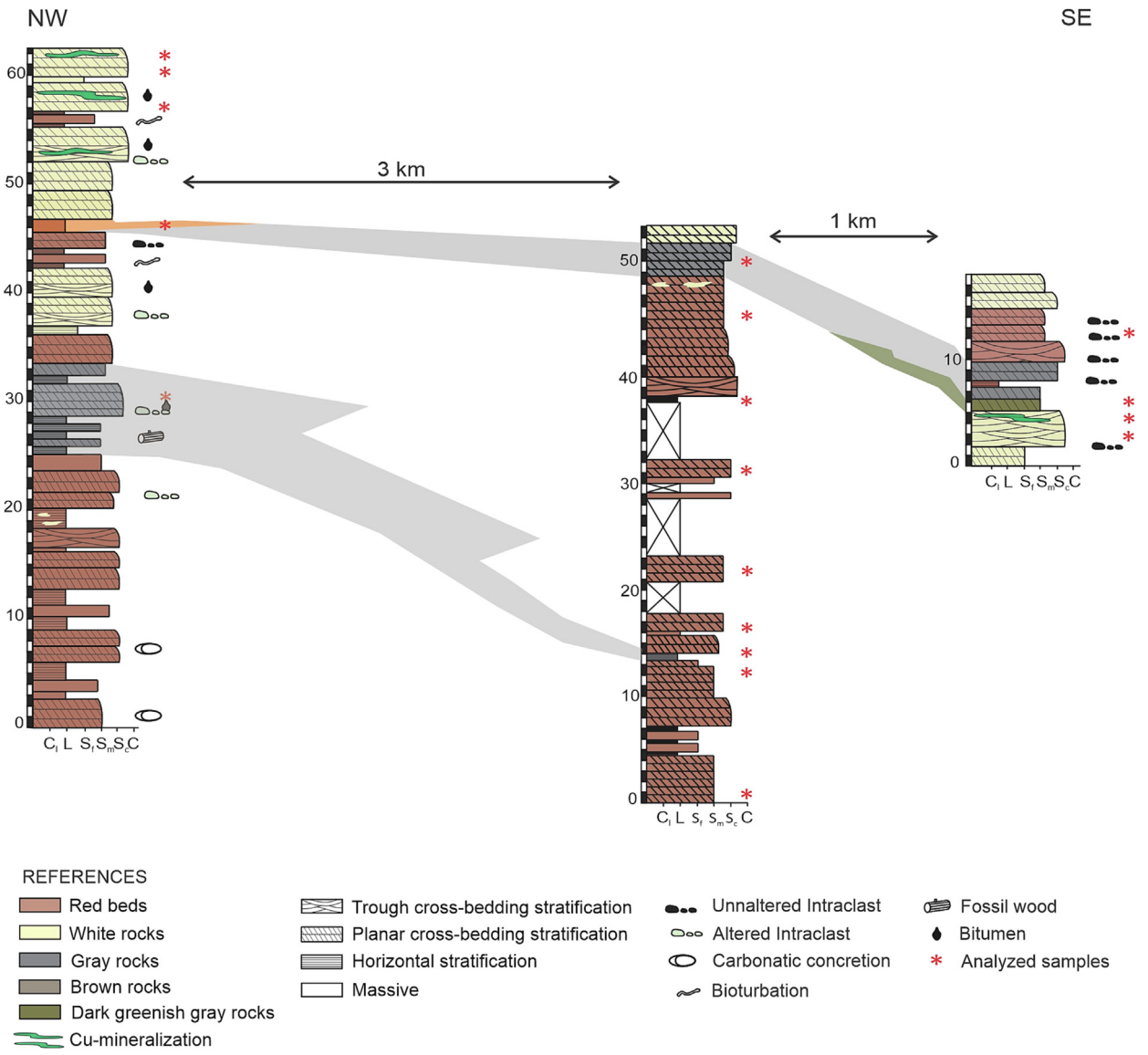


Fig. 4. Stratigraphic profiles of the Huincul Formation showing the distribution of red, white, gray, brown and dark greenish gray sandstones which characterized the redox system. The redox front which comprises the main vanadium orebody has been marked through stratigraphic profiles correlation. (For interpretation of the references to color in this figure legend, the reader is referred to the web version of this article.)

by secondary V-bearing hematite. This last mineral, together with smectite, gives the gray color to the sandstone. Vanadium-bearing hematite also occurs as replacement of detrital Ti-magnetite (Fig. 7d). In some cases, V-bearing chlorite-smectite mixed-layer minerals and more rarely illite–smectite mixed-layer minerals occur with smectite in the gray sandstone. When chlorite-smectite mixed-layer minerals predominate, sandstone turns to tan color defining the brown sandstone (Rainoldi et al., 2014). Coatings of V-bearing hematite were also identified at the surface of the chlorite-smectite mixed-layer minerals and both are impregnated with bitumen (Fig. 7e). Also, local occurrence of an undetermined Mn oxide has been observed associated with chlorite-smectite mixed-layer minerals (Fig. 7f). In some cases, the transition to the white sandstone is marked by the presence of V(Cu)-rich chlorite which gives to the rock a dark greenish gray color (Fig. 6a). The dark greenish gray and brown sandstones with chlorite and chlorite-smectite mixed-layer minerals, respectively, represent the most reducing portion of the redox front. Vanadium-chlorite occurs as grains coatings and filling the pore space (Fig. 7g, i). Vanadium-hematite has been identified accompanying V-chlorite (Fig. 7h, i). At the contact of the dark greenish gray with the white sandstones, in association with the Cu mineralization just behind the redox front, chlorite occurs as spherulitic aggregates (Fig. 7j, k) and have a very low V content that is counter balanced by increase in Cu, Fe and Mg, (i.e., transition from V(Cu)-rich chlorite to Cu-rich chlorite).

The deposit is affected by supergene alteration of the ore, where hypogene chlorite and copper sulfides are replaced by secondary vanadium and copper minerals (Fig. 7l–o). The V supergene minerals include vanadates like volborthite $Cu_3(V_2O_7)(OH)_2{\cdot}2H_2O$ and vésigniéite $BaCu_3(VO_4)_2(OH)_2$ (Fig. 7l), gamagarite $Ba_2(Fe^{3+},Mn^{3+})(VO_4)_2(OH)$ (Fig. 7m) and uranovanadates like francevillite (Ba, Pb)$(UO_2)_2V_2O_8{\cdot}5(H_2O)$ and carnotite $K_2(UO_2)_2(VO_4)_2{\cdot}3H_2O$. At the contact with the white sandstone, where pyrite is strongly oxidized, V commonly occurs associated with secondary Cu-Fe-V oxides (Fig. 7n). When Cu-chlorite predominates, malachite fills

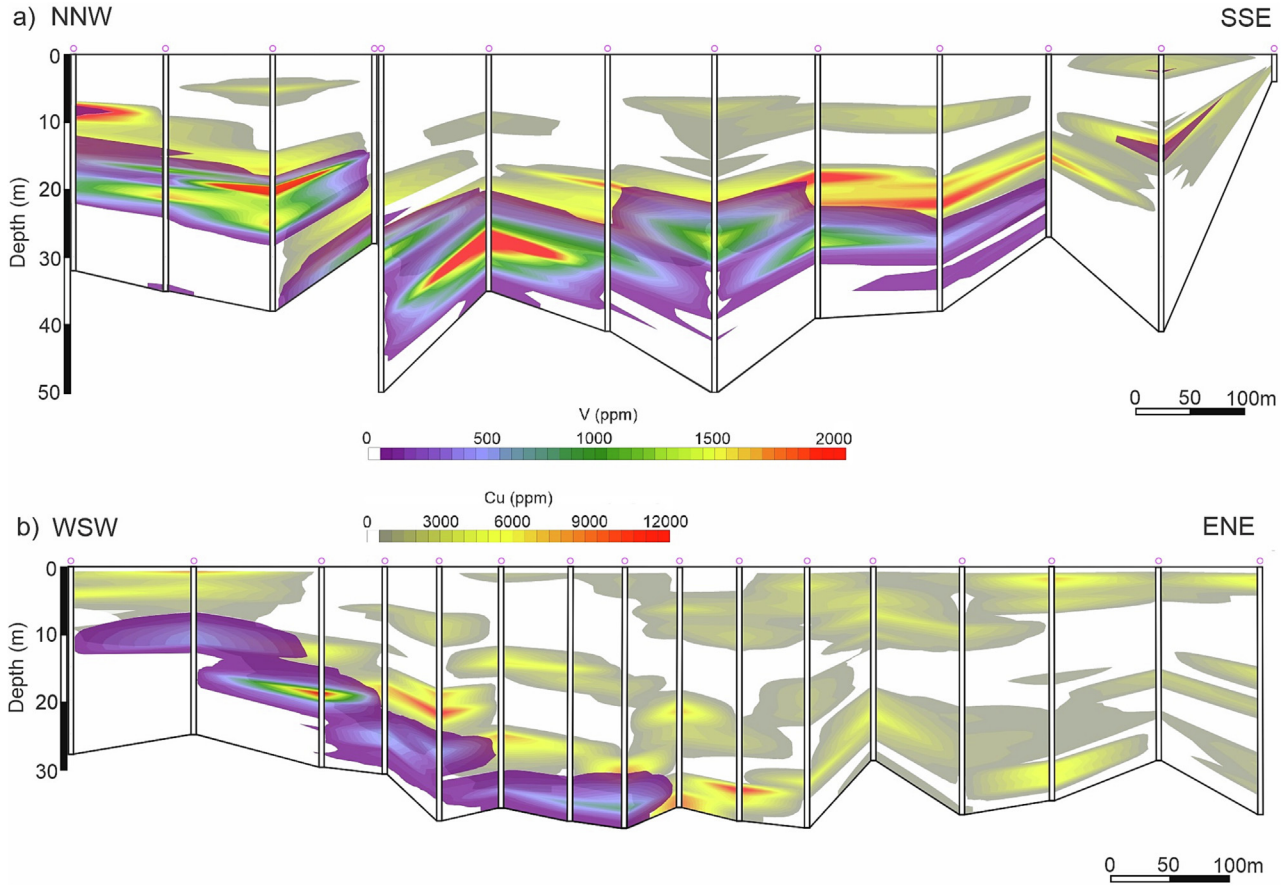


Fig. 5. NNW–SSE and WSW–ENE cross sections showing the distribution of V and Cu in the Los Chihuidos deposit. Vanadium has been superimposed to copper distribution in order to show that vanadium always occurs below copper orebody. Geochemical data provided from Orion del Sur S.A.

the interstitial space between chlorite crystals (Fig. 7o). Anomalies of U are more erratic and are always associated with supergene V ore. Scarce microfractures filled with baryte postdates vanadates and uranovanadates.

5.3. Characterization of vanadium minerals

5.3.1. V-bearing Dioctahedral smectite

Smectite was identified from X-ray typical diffraction patterns with d(001) at 15.1 Å in air dried conditions which expands to 16.9 Å after ethylene–glycol (EG) solvation and the occurrence of five rational suborder basal reflections (Fig. 8a, b). The XRD pattern of randomly oriented preparation of smectite shows d(060) peak close to 1.5 Å with a correlative b-axis of about 8.9–9 Å, typical of dioctahedral clay minerals. Mid infrared spectra of smectite (Fig. 9a) is similar to those given for montmorillonite in the literature (Madejová et al., 2011). The broad band near 3392 cm^{-1} is due to O–H stretching vibrations of adsorbed water. The octahedral sites of the montmorillonite are occupied by Al^{3+} partly substituted by Fe^{3+} and Mg^{2+}, as evidenced by the position of the bands in the OH-bending region: 914 cm^{-1} (Al_2OH), 874 cm^{-1} ($AlFe^{3+}OH$), and 841 cm^{-1} (AlMgOH). The chemical analysis of smectite (Table 2) indicate the presence of these cations supporting the infrared characterization. Because of their similarity of mass and ionic radius, Fe and V would produce similar spectral effects (Whitney and Northrop, 1986) and V could substitute significant amounts of Fe in octahedral sites. Microchemical analysis of smectite correspond to that of montmorillonite (Fig. 10a) with contents of V and Cu which vary from 0.2 wt.% to 1 wt.% V_2O_3, 0.3 wt.% to 0.8 wt.% CuO in white sandstones and of 1.4–2.2 wt.% V_2O_3, 0.1–0.2 wt.% CuO in gray sandstones (Table 2).

5.3.2. V-bearing hematite

Hematite in the gray sandstone occurs as aggregates of subhexagonal plates or replacing detrital martitized titanomagnetite (Fig. 7d); partial replacement of Fe by V in detrital Fe-Ti minerals has been also observed in other sandstone-hosted uranium-vanadium deposits (Schmid et al., 2020). Microchemical analysis of secondary hematite also indicate V_2O_3 content between 1.31 wt.% and 9.01 wt.%. In detrital martitized titanomagnetite, chemical analysis show Ti content in magnetite and V in hematite (Table 3). In the brown sandstone, hematite microchemical analysis indicate lower V and higher Mn contents compared to hematite host in the gray sandstone. Manganese has been also detected in bitumen impregnations that covers chlorite-smectite mixed-layers and hematite, and more rarely in a secondary Mn oxide that occurs associated with chlorite-smectite mixed-layers (Fig. 7e; Table 3).

5.3.3. V-bearing illite–smectite mixed-layer minerals

Minor amounts of illite–smectite mixed-layers were identified by its (001) reflection close to that of smectite, in both air dry and ethylene glycol states. However, the absence of rationality of the (002) reflection after ethylene glycol saturation is indicative of a random illite–smectite mixed-layer minerals (R0) which (002) reflection occurs at intermediate position between that of discrete smectite at 8.5 Å and that of discrete illite at 10 Å. Microchemical analysis of the illite–smectite mixed-layer minerals

Table 1
Whole rock chemical composition (in wt.% and ppm) of representative samples of the Los Chihuidos SSC deposit.

	Red sandstones								Gray sandstones								White sandstone								Brown stn.	Cu-chlorite-rich sandstone				Cu-Ore sandstone	
Sample ID	Gr3	Gr11	SS135	SS136	SS139	SS146	SS1*	SS6*	SS68*	SS74*	Gr7	SS143	SS145	SS7*	SS77*	SS16*	Gr5	Gr10	SS134	SS147	SS11*	SS12a*	SS15*	SS17*	SS79*	SS93*	Gr2	SS181	SS241	SS9	SS92a	SS92b
SiO_2	75.31	81.28	71.92	76.22	73.82	82.41	66.96	78.24	74.64	78.18	81.70	78.33	78.38	76.43	75.59	82.25	73.36	82.75	75.27	79.65	84.33	66.46	85.53	72.18	82.24	77.75	64.27	65.58	65.13	79.54	50.68	68.03
Al_2O_3	12.18	9.76	12.28	11.37	13.31	9.39	11.83	10.88	12.09	9.89	10.01	11.78	10.87	11.13	12.41	8.65	9.57	8.79	7.92	9.51	8.55	6.25	8.07	6.54	8.68	10.43	6.06	8.43	6.92	8.86	8.85	10.91
TiO_2	0.35	0.21	0.37	0.41	0.56	0.19	0.49	0.28	0.39	0.20	0.18	0.32	0.24	0.39	0.26	0.15	0.63	0.15	0.11	0.27	0.13	0.09	0.10	0.093	0.20	0.295	0.103	0.149	0.114	0.151	0.644	0.194
FeO	0.70	1.20	0.80	1.00	1.00	1.10	0.22	0.47	0.89	0.54	0.40	0.90	1.10	0.74	0.79	1.13	1.00	0.30	1.00	1.10	0.14	0.22	0.76	0.1	0.76	0.33	0.8	1.41	1.67	0.73	0.48	0.54
Fe_2O_3	1.71	1.08	2.09	1.39	2.52	0.85	3.36	1.76	1.19	0.85	0.74	1.43	1.07	1.68	1.52	0.91	0.17	0.94	0.62	0.53	0.53	0.25	0.41	0.59	0.33	0.36	2.87	4.85	1.36	< 0.01	2.64	6.64
MnO	0.05	0.02	0.05	0.13	0.04	0.02	0.12	0.02	0.04	0.02	0.02	0.03	0.02	0.02	0.02	0.03	0.15	0.02	0.20	0.03	0.13	0.10	0.01	0.147	0.01	0.091	0.012	0.181	0.111	0.012	0.015	0.011
CaO	2.10	0.72	2.36	0.80	1.22	0.77	5.68	0.78	1.77	1.55	0.99	0.84	0.83	0.90	1.14	0.71	6.02	1.25	6.08	0.73	0.61	12.90	0.61	9.5	1.46	0.91	0.67	0.69	0.59	0.7	0.92	0.83
MgO	0.43	0.53	0.55	0.27	0.40	0.34	0.30	0.36	0.46	0.23	0.30	0.37	0.40	0.52	0.71	0.99	0.29	0.37	0.24	0.48	0.16	0.11	0.20	0.25	0.52	0.44	0.35	1.18	0.75	0.23	0.5	0.24
Na_2O	4.12	3.41	4.58	5.02	5.01	3.08	4.50	3.79	4.73	3.78	3.46	4.44	3.70	3.57	3.95	2.35	3.53	2.95	2.08	3.07	2.68	2.14	2.61	2.01	2.69	3.13	1.63	1.77	1.6	2.92	1.5	2.99
K_2O	1.11	1.16	1.05	1.10	1.06	1.16	0.93	1.05	1.19	1.21	1.34	0.95	1.01	1.12	1.28	1.39	0.85	1.08	1.56	1.11	1.25	0.99	1.35	1.23	1.38	1.05	0.54	1.11	0.92	1.14	0.76	1.15
P_2O_5	0.06	0.03	0.08	0.06	0.08	0.04	0.11	0.03	0.07	0.05	0.05	0.06	0.06	0.06	0.04	0.05	0.06	0.48	0.04	0.05	0.03	0.03	0.03	0.04	0.04	0.07	0.04	0.09	0.09	0.05	0.16	0.13
LOI	2.67	1.30	2.64	3.24	1.83	1.41	4.96	1.22	1.72	1.46	1.44	1.40	2.38	2.13	3.04	2.20	5.13	1.49	5.48	1.71	1.27	10.44	1.07	8.18	2.27	3.86	8.53	7.27	7.96	3.19	13.4	6.12
Total	100.78	100.71	98.77	100.41	100.85	100.76	99.49	98.93	99.27	98.02	100.63	100.84	100.06	98.78	100.80	100.90	100.76	100.57	100.59	98.24	99.83	100	100.80	100.9	100.70	98.72	85.96	92.86	87.4	97.48	80.549	97.78
CO_2	1.01	0.07	1.09	0.05	0.15	0.04	3.59	0.02	0.77	0.67	0.22	0.03	0.04	<0.01	0.22	0.03	4.05	0.05	4.15	0.04	0.02	9.61	0.02	7.01	0.52	0.07	0.9	1.27	1.85	0.12	1.18	0.19
S	0.02	0.01	0.02	0.02	0.01	<0.01	n.d.	n.d.	0.02	0.02	0.01	0.02	<0.01	n.d.	0.03	n.d.	0.01	0.02	<0.01	0.07	n.d.	n.d.	n.d.	n.d.	0.14	<0.01	0.31	n.d.	n.d.	n.d.	0.05	0.2
Zr	108	77	114	93	141	82	105.00	108	164	77.00	83	116	103	141.00	97.00	87.00	144	75	65	90	80.00	61	61	78	76.00	119	47	94	67	85	340	93
Cu	30	20	10	30	20	10	20	260	40	20	320	< 10	10	880'	30	710	200	50	130	< 10	670	1430	30	31.20	60	246,000	106,000	66,800	90,100	18,400	158,000	30,700
V	244	341	77	63	91	80	89	84	45	53	1840	298	263	59	817	61	825'	32	63	112	30	17	32	25	29	65	2516	641	403	102	222	266
U	3.85	2.26	1.78	1.8	1.64	2.13	1.55	2.17	1.95	1.33	3.74	3.25	3.59	3.5	5.02	4.55	4.55	3.71	3.8	2.13	4.75	3.31	1.35	2.11	1.82	27.8	24.7	20.8	29.5	6.7	250.0	42.1
La	20.5	22.7	21.3	16.1	20.8	22.3	15.4	17.20	27.00	20.00	222	21.5	22	18.50	19.20	19.40	19.5	20.8	18.2	18.2	19.2	14.30	16.80	18.7	21.00	14.9	13.1	17.7	13	15.7	16.9	12.9
Ce	38.2	44.9	41.6	32.8	40.8	41.4	32.2	32.2	50.5	38.8	43.3	42.1	40.6	34.8	35.9	37.4	38.7	42.6	33.3	36	40.5	29.7	32.8	36	41.6	28.4	27.5	33.2	25.8	31.4	32.7	23.9
Pr	4.43	5.07	4.9	3.75	4.71	4.65	3.69	3.58	6.56	4.84	4.83	4.95	4.66	3.79	4.41	4.06	4.4	5.4	3.74	3.82	4.4	3.2	3.51	3.97	4.92	3.44	3.11	3.67	2.72	3.44	3.82	2.99
Nd	16.5	18.8	18.3	14	17.6	16.9	14.3	13.3	24.4	18.2	17	17.5	17.1	14.3	16.2	14.6	16.5	22.1	13.6	13.8	16.9	12	13	14.6	18.4	12.7	12	13.5	10.1	12.8	14.5	11.8
Sm	3.13	3.33	3.48	2.67	3.47	3.03	2.84	2.38	4.37	3.31	3.09	3.12	3.1	2.57	3.02	2.78	3.18	5.36	2.62	2.57	3.15	2.25	2.3	2.76	3.46	2.45	2.25	2.72	1.99	2.61	3.12	2.94
Eu	0.778	0.782	0.893	0.761	0.83	0.705	0.795	0.616	0.935	0.776	0.752	0.757	0.724	0.694	0.773	0.633	0.799	1.46	0.634	0.578	0.787	0.576	0.552	0.625	0.765	0.601	0.513	0.582	0.454	0.661	0.666	0.759
Gd	2.28	2.54	2.78	2.19	2.9	2.24	2.24	1.79	3.03	2.47	2.42	2.6	2.39	1.89	2.36	1.86	2.63	5.82	2.23	1.99	2.37	1.79	1.71	2.17	2.42	1.88	1.74	2.26	1.63	2.34	3.15	2.81
Tb	0.37	0.35	0.4	0.34	0.42	0.32	0.33	0.26	0.46	0.37	0.33	0.38	0.35	0.28	0.39	0.27	0.46	0.93	0.38	0.31	0.35	0.26	0.24	0.34	0.37	0.35	0.29	0.36	0.28	0.41	0.67	0.54
Dy	2.02	1.82	2.28	1.97	2.4	1.58	1.93	1.56	2.39	1.86	1.78	2.07	1.88	1.67	2.18	1.58	2.51	4.54	2.22	1.71	2.01	1.48	1.36	2.01	1.94	1.94	1.6	2.19	1.66	2.59	4	2.76
Ho	0.41	0.36	0.47	0.41	0.47	0.31	0.38	0.32	0.48	0.38	0.37	0.44	0.38	0.34	0.47	0.3	0.5	0.81	0.45	0.37	0.37	0.27	0.26	0.39	0.38	0.41	0.31	0.42	0.3	0.51	0.8	0.53
Er	1.17	1.08	1.39	1.16	1.38	0.93	1.11	1.01	1.4	1.14	1.07	1.29	1.17	1.11	1.45	0.92	1.47	1.92	1.32	1.09	1.09	0.78	0.81	1.08	1.13	1.16	0.83	1.18	0.88	1.48	2.28	1.41
Tm	0.185	0.165	0.208	0.177	0.21	0.145	0.165	0.164	0.232	0.174	0.162	0.209	0.188	0.18	0.228	0.145	0.222	0.261	0.196	0.17	0.163	0.12	0.122	0.158	0.182	0.19	0.12	0.174	0.135	0.223	0.358	0.216
Yb	1.3	1.14	1.42	1.18	1.38	0.95	1.21	1.11	1.52	1.1	1.12	1.41	1.28	1.21	1.54	0.99	1.47	1.6	1.3	1.18	1.14	0.83	0.83	1.03	1.2	1.2	0.78	1.17	0.89	1.41	2.27	1.32
Lu	0.21	0.182	0.237	0.184	0.22	0.157	0.2	0.186	0.231	0.163	0.183	0.232	0.206	0.209	0.227	0.173	0.239	0.234	0.209	0.202	0.186	0.137	0.142	0.173	0.177	0.183	0.123	0.186	0.142	0.231	0.353	0.192

* Samples from Rainoldi et al. (2014).

formed in the gray sandstone (Fig. 10a) indicate vanadium content approximatively twice higher (4–4.6 wt.% V_2O_3) than in the associated montmorillonite (2.2 wt.% V_2O_3) while the CuO content remains <0.3 wt.% (Table 2).

5.3.4. V-Cu bearing chlorite-smectite mixed-layer minerals (corrensite-type)

X-ray diffractograms of the oriented preparations of Ca saturated clay fraction agree with a regularly ordered chlorite-smectite mixed-layers mineral with basal reflections broadly similar to those of corrensite. It is characterized by a superlattice reflection at ~ 29 Å expanding to ~ 31 Å after ethylene glycol solvation (EG), and the occurrence of several rational suborder basal reflections (Bailey, 1982) (Fig. 8c). The position of the (060) reflection near 1.53 Å indicates that the mixed layer mineral is trioctahedral on average (b-axis close to 9.2 Å). In the gray sandstone, a weak reflection at 14.8 Å strongly overlapped by the main reflection of smectite, after EG solvation of oriented clay preparation suggests the presence of minor amounts of this corrensite-type mineral (Fig. 8b). Infrared absorption spectra of corrensite-type minerals overlap those of the respective constituents of each clay minerals (Oinuma and Hayashi, 1965) (Fig. 9b). The broad band near 3565 cm^{-1} is attributed to the interlayer OH groups in chlorite. Bending vibrations of the OH bound to octahedral cations are observed at ~914 cm^{-1} for Al_2OH, ~885 cm^{-1} for $AlFe^{3+}OH$, ~839 cm^{-1} for AlMgOH and ~810 cm^{-1} for $Fe_2^{3+}OH$, which correspond to the presence of dioctahedral clay minerals as smectite, kaolinite or Al-rich chlorite; considering the close relationship of corrensite-type clay mineral and montmorillonite at the redox front, and that montomorillonite presents bands at 914 cm^{-1} (Al_2OH), 874 cm^{-1} ($AlFe^{3+}OH$), and 841 cm^{-1} (AlMgOH) it is suggested that these bands corresponds to the smectite fraction in the corrensite-type clay mineral. The strong complex band at ~ 687–660 cm^{-1} bending vibrations of the OH bound to octahedral cations in trioctahedral clay minerals (e.g., Madejová et al., 2011) and reveal here chlorite (Oinuma and Hayashi, 1965). The chemical data of this corrensite-type mineral do not really agree with those of a true corrensite. Compared to corrensite, it is aluminum-rich and contains significant amounts of V and Cu (1.2–2.4 wt.% V_2O_3, 1.2–2 wt.% CuO in gray sandstone and 0–0.08 wt.% V_2O_3, 0.5–0.8 wt.% CuO in brown sandstone; Table 2). The structural formulas of this mineral (calculated on the basis of 25 oxygens) are characterized by octahedral occupancy near 8 instead of 9 for that of a true corrensite which is a regular mixed-layer clay mineral containing trioctahedral chlorite (50%) and trioctahedral smectite (50%). This could be indicative either of intimate mixture of an Al-rich clay mineral (such as kaolinite) with corrensite or the presence of a dioctahedral sheet in one of the layer component of the mixed-layer mineral (smectite or chlorite). The fact that the compositional field of this mixed-layer mineral fall near mid-distance between those of saponite and di-trioctahedral chlorite and not between those of saponite and tri- trioctahedral chlorite, when plotted in the MR_3-$2R^3$-$3R^2$ chemiographic diagram of clay minerals (Fig. 10), argues for a di-trioctahedral composition of the chlorite component in the corrensite-type mineral.

5.3.5. V(Cu)-rich di-trioctahedral chlorite

Chlorite was identified in XRD of the ore samples (Fig. 6) by the (001) reflection at 14.3 Å, which did not shift after ethylene glycol treatment, and the following two suborder basal reflections (Fig. 8d). From mid infrared spectra it is possible to see that many of the absorption bands of this chlorite matches with the absorption bands of di-trioctahedral V-chlorite from the literature which fall between those of the roscoelite ($KA1V_2Si_3O_{10}(OH)_2$) and clinochlore ($(Mg, Fe^{2+})_5Al(Si_3Al)O_{10}(OH)_8$), both in position and intensity (Fig. 9c) (Whitney and Northrop, 1986). The position of the main

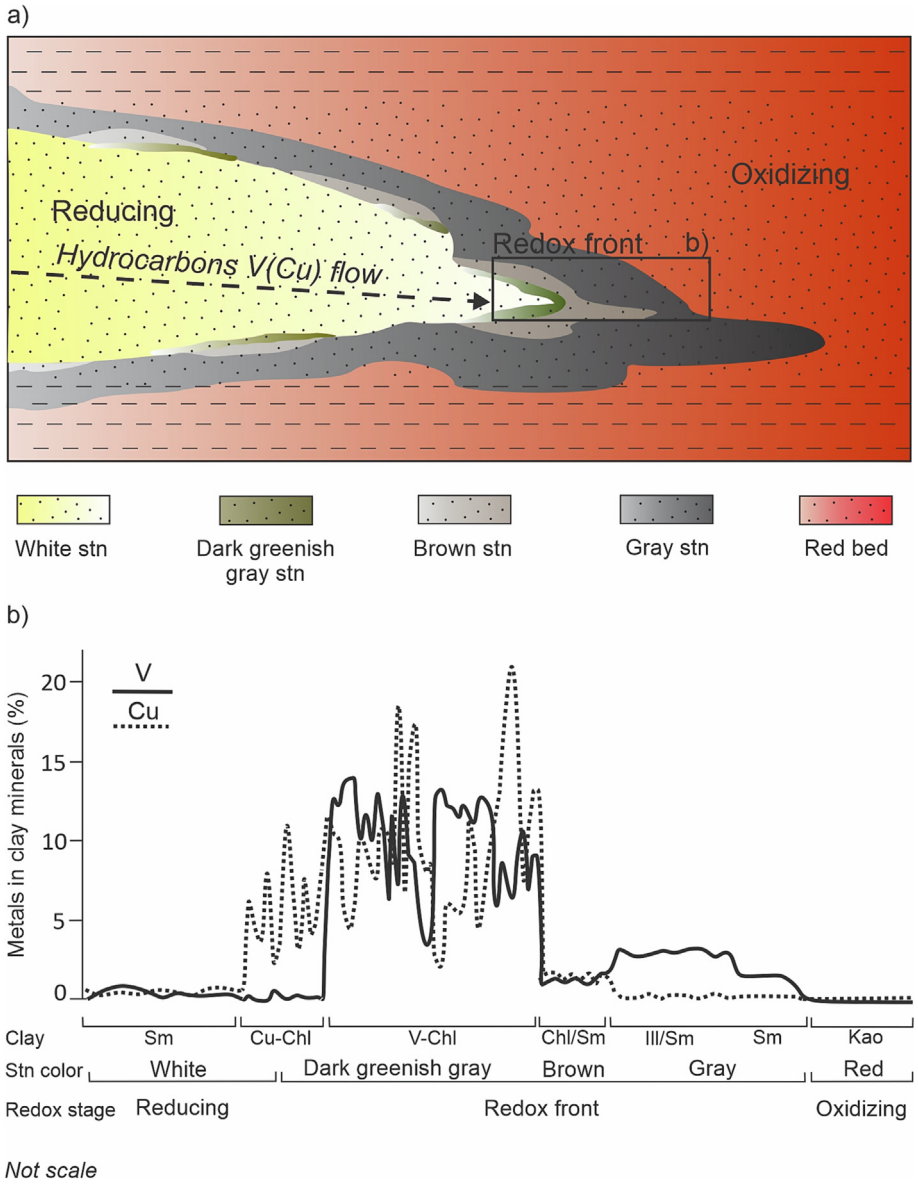
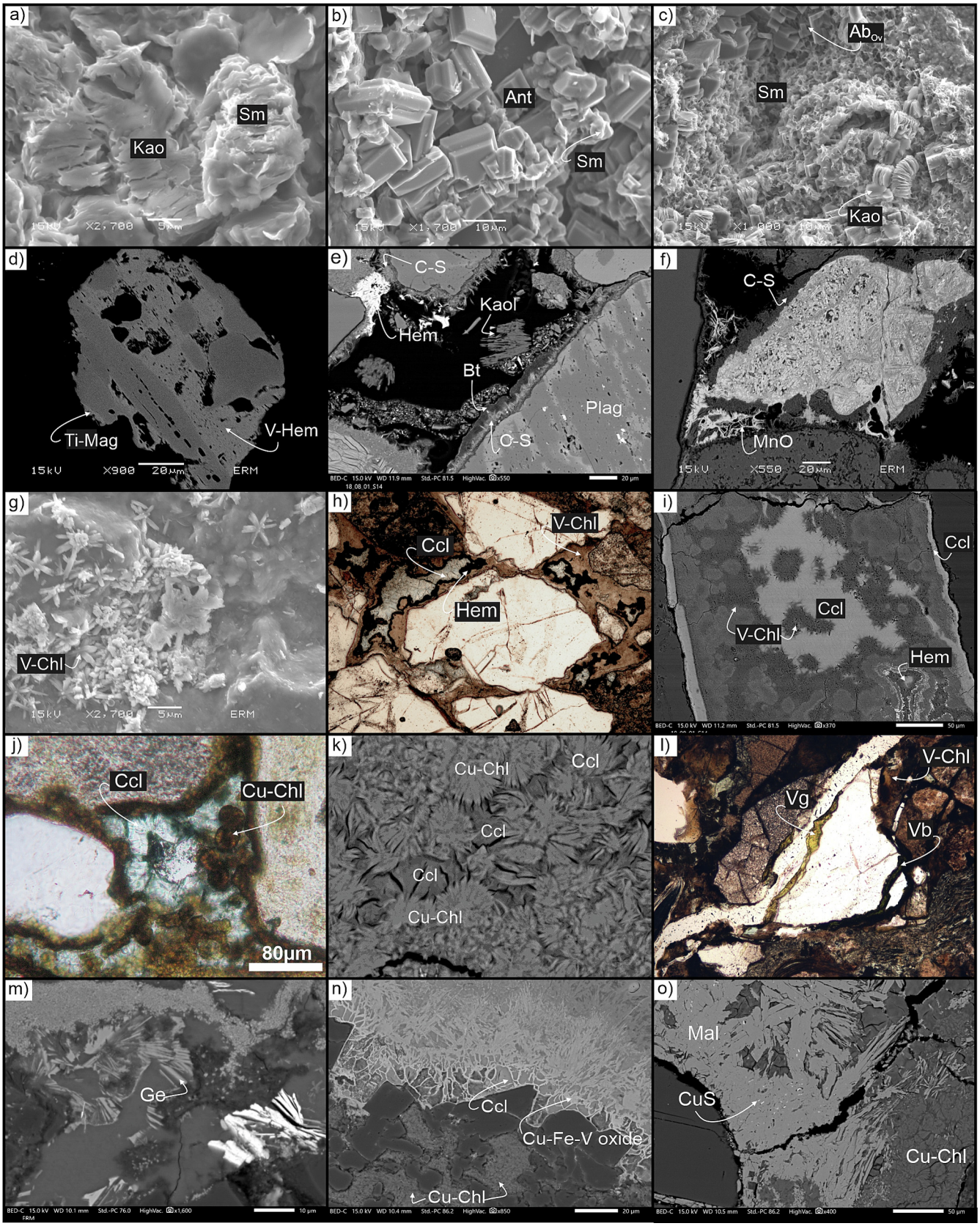


Fig. 6. Redox front model of the Los Chihuidos deposit. **(a)** Model with distribution of the diagenetic facies defined in the redox system. **(b)** Zoning of clay minerals and their V and Cu contents at the different redox stages of the Los Chihuidos deposit.

OH band at 3591 cm^{-1} suggests that significant amounts of Fe and/or V occupy octahedral sites. Bending vibrations of the OH bound to octahedral cations are observed at ~914 cm^{-1} for Al_2OH and ~877 cm^{-1} for $AlFe^{3+}OH$, typical of dioctahedral phyllosilicates. The strong absorption band at 517 cm^{-1} is typical of dioctahedral Al rich phyllosilicates, as observed in other di-trioctahedral V-chlorites (Whitney and Northrop, 1986). The di-trioctahedral layer silicate structure is evidenced by the bands at 451 cm^{-1} and 468 cm^{-1} as in sudoite (Madejová et al., 2011). The strong complex band at ~651 cm^{-1} to 685 cm^{-1} is due to trioctahedral configuration in chlorite. Microchemical analyses confirm the di-trioctahedral characteristics of this chlorite (octahedral occupancy near 5 cations for 14 oxygens) with high concentrations of V (6.3–16.1 wt.% V_2O_3) and Cu (1.9–18.7 wt.% CuO) (Fig. 10; Table 2).

Fig. 7. Microphotographs of diagenetic minerals from the altered and mineralized sandstones. White sandstone: **(a)** Kaolinite partially dissolved and replaced by smectite. **(b)** Anatase associated with smectite filling the pore space. Gray sandstone: **(c)** Smectite replacing previous kaolinite and filling the pore space. **(d)** Detrital titanomagnetite partially replaced by V-hematite. Brown sandstone: **(e)** Chlorite-smectite mixed-layers coating detrital grains associated with bitumen impregnations and secondary hematite. **(f)** Chlorite-smectite mixed-layers associated with secondary manganese oxide. Dark greenish gray sandstone: **(g)** Vanadium chlorite filling the pore space. **(h,i)** Vanadium rich hematite associated with vanadium chlorite and chrysocolla. Copper mineralized sandstones: (**j**) Copper chlorite in spherulitic aggregates. **(k)** Interstitial spaces within copper chlorite filled with chrysocolla. Oxidized vanadium minerals in dark greenish gray sandstones: **(l)** Vésigniéite and volborthite filling intragranular microcraks. **(m)** Gamagarite filling intergranular pore space. Oxidized copper-vanadium minerals in copper mineralized sandstones: **(n)** Abundant Cu-Fe-V oxides after pyrite oxidation. **(o)** Malachite associated with Cu-chlorite. *AbOv: albite overgrowth; Ant: anatase; Bt: bitumen; Ccl: chrysocolla; C-S: chlorite-smectite; CuS: copper sulfide; Cu-Chl: copper chlorite; Ge: gamagarite; Kao: kaolinite; Mal: malachite; MnO: manganese oxide; Plag: plagioclase; QzOv: quartz overgrowth; Sm: smectite; Ti-Mag: titanium magnetite; Vb: volborthite; Vg: vésigniéite; VF: volcanic fragment; V-Chl: vanadium chlorite; V-Hem: vanadium hematite.*


a)
Sm
Kao
15kV X2,700 5µm
b)
Ant
Sm
15kV X1,700 10µm
c)
Ab$_{ov}$
Sm
Kao
15kV X1,000 10µm
d)
Ti-Mag
V-Hem
15kV X900 20µm ERM
e)
C-S
Kaol
Hem
Bt
Plag
C-S
BED-C 15.0 kV WD 11.9 mm Std.-PC 81.5 HighVac. x550 20 µm
18_08_01_S14
f)
C-S
MnO
15kV X550 20µm ERM
g)
V-Chl
15kV X2,700 5µm ERM
h)
V-Chl
Ccl
Hem
i)
Ccl
Ccl
V-Chl
Hem
BED-C 15.0 kV WD 11.2 mm Std.-PC 81.5 HighVac. x370 50 µm
j)
Ccl
Cu-Chl
80µm
k)
Cu-Chl
Ccl
Ccl
Ccl
Cu-Chl
l)
V-Chl
Vg
Vb
m)
Ge
BED-C 15.0 kV WD 10.1 mm Std.-PC 76.0 HighVac. x1,600 10 µm
FRM
n)
Ccl
Cu-Fe-V oxide
Cu-Chl
BED-C 15.0 kV WD 10.4 mm Std.-PC 86.2 HighVac. x850 20 µm
o)
Mal
CuS
Cu-Chl
BED-C 15.0 kV WD 10.5 mm Std.-PC 86.2 HighVac. x400 50 µm

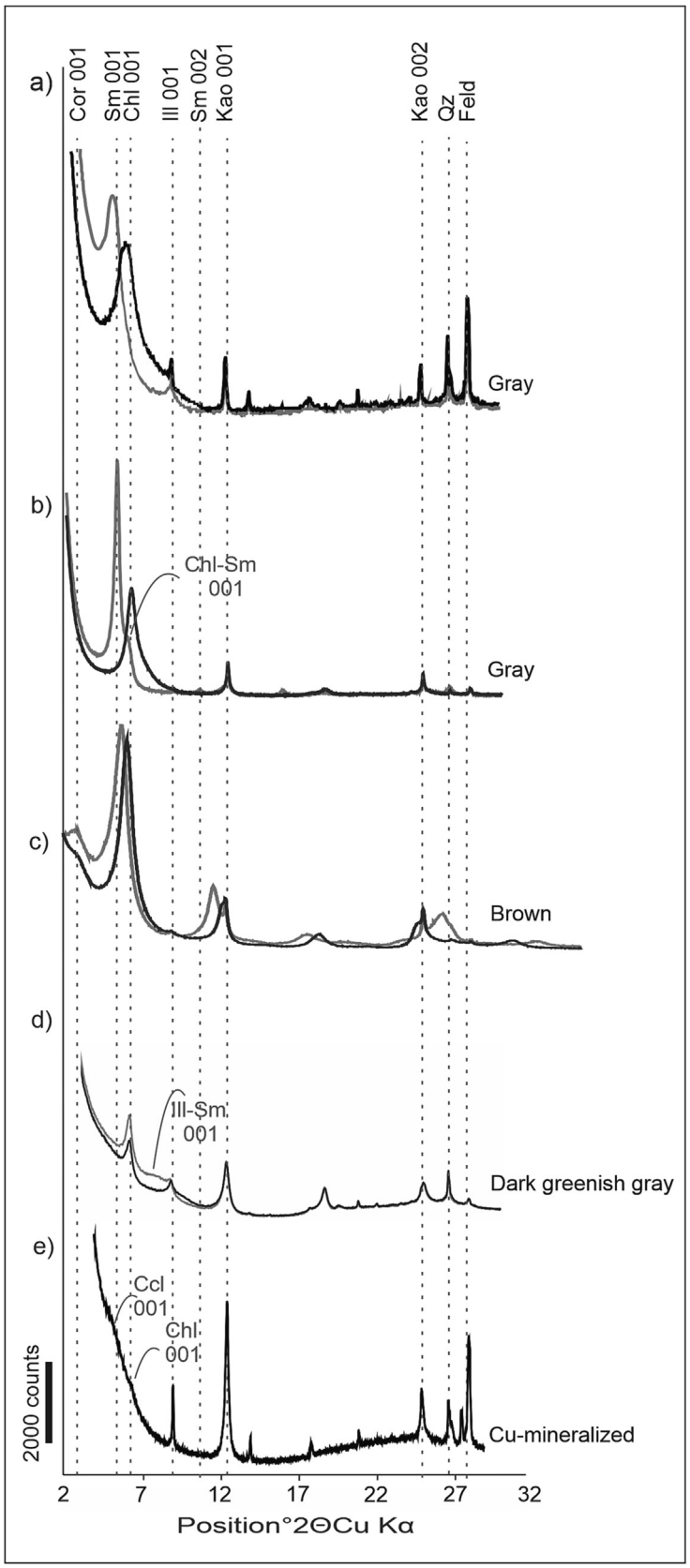


Fig. 8. X-Ray diffraction patterns. Kaolinite is always present because is precipitated early in the original red bed strata. (a–d) Identification of clay minerals into the redox front. Smectite predominates in gray sandstones with minor illite–smectite and chlorite-smectite mixed-layers, chlorite-smectite mixed-layers predominates in the brown sandstones, and chlorite and minor illite–smectite mixed-layers in the dark greenish gray sandstone. The dark greenish gray sandstone is hardly indurated avoiding clay minerals release, resulting in the small intensity in the diffractogram peaks. (e) Clay minerals into copper mineralized sandstone with chlorite; the peak of chrysocolla is only slightly developed due to the low crystallinity of the mineral.

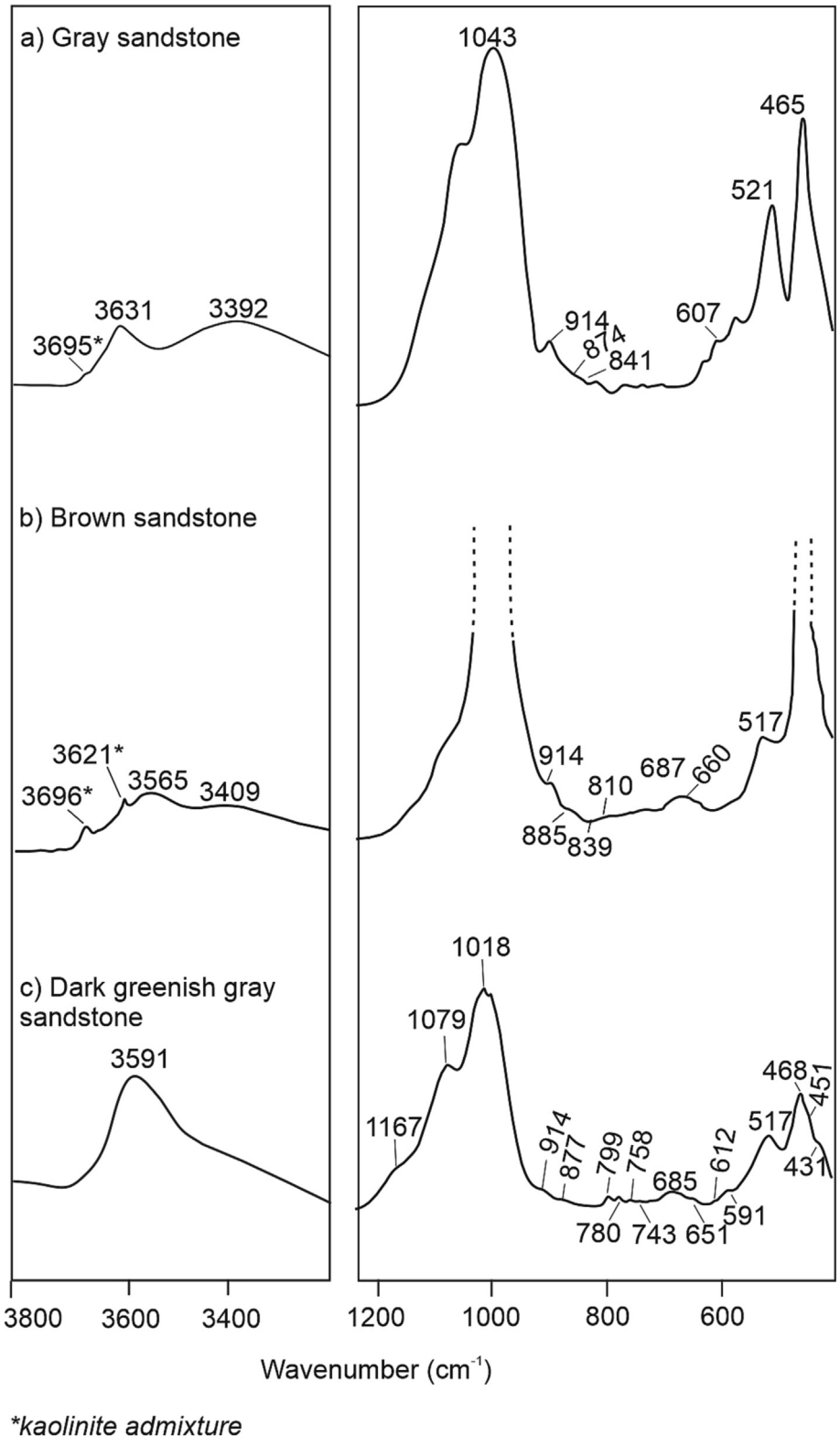


Fig. 9. Infrared spectra of characteristic clay minerals of the Los Chihuidos deposit. (a) In gray sandstone infrared spectra matches with montmorillonite. (b) In brown sandstone, infrared spectra presents the bands belonging to chlorite and smectite due to the presence of chlorite-smectite mixed-layers. Dashed line indicates oversaturation (c) In dark greenish gray sandstone, infrared spectra fix with di-trioctahedral chlorite.

5.3.6. Cu(V)-rich tri-trioctahedral chlorite

Such a type of tri-trioctahedral chlorite is V-poor compared with the aforementioned di-trioctahedral chlorites. Tri-trioctahedral chlorite-rich rocks are hardly indurated interfering in clay extraction. Due to this, only a slight and broad peak at ~14 Å was identified in X-ray diffractograms (Fig. 8e). Structural formulas of spherulitic chlorite aggregates in Cu-mineralized sandstones (Fig. 10; Table 2) indicate an octahedral occupancy of

Table 2
Representative analyses of clay minerals.

	White		Gray						Brown		Dark greenish gray							
	Smectite				I/S		Corrensite				Di-trioctahedral chlorite				Tri-trioctahedral chlorite			
wt.%	Gr5-5	Gr5-3	Gr7-18	Gr7-17	Gr7-8	Gr7-3	SS7-38	SS7-39	SS16-2	SS16-9	SS41-2	SS41-4	SS64-2	SS64-3	SS24-1	SS24-2	SS24-3	SS24-4
Na_2O	0.27	0.26	0.84	0.75	0.20	0.22	0.44	0.42	0.45	0.25	0.00	0.00	0.00	0.00	0.16	0.14	0.18	0.15
MgO	3.04	3.01	2.59	2.57	2.02	2.02	11.73	12.04	10.07	9.50	13.97	12.39	10.34	11.76	5.13	6.49	4.20	4.39
Al_2O_3	17.85	18.77	22.21	22.07	12.46	13.04	18.36	17.98	13.53	12.70	21.54	19.52	15.86	16.31	14.03	15.26	14.03	13.98
SiO_2	47.90	48.72	48.17	47.76	36.45	38.10	42.15	39.45	31.11	29.50	34.54	34.50	30.63	29.91	27.14	25.64	28.00	28.25
K_2O	1.22	2.66	3.39	3.42	4.49	3.95	0.66	0.66	1.01	0.70	0.13	0.26	0.80	0.68	0.00	0.02	0.01	0.00
CaO	1.64	1.34	0.63	0.60	0.53	0.55	0.34	0.38	0.25	0.45	0.11	0.27	0.24	0.26	0.12	0.10	0.15	0.19
TiO_2	0.05	0.03	0.07	0.12	0.03	0.08	0.06	0.04	0.09	0.00	0.00	0.05	0.00	0.00	0.00	0.00	0.00	0.00
V_2O_3	0.23	1.06	2.12	2.18	4.66	3.94	2.41	2.11	0.03	0.02	13.18	13.90	16.05	14.81	0.00	0.57	1.55	1.72
MnO	0.07	0.00	0.00	0.04	0.01	0.08	0.11	0.01	0.11	0.12	0.00	0.05	0.00	0.07	0.82	1.02	0.17	0.13
FeO	1.63	2.58	1.87	2.04	1.78	1.80	7.13	7.11	10.85	10.09	2.11	2.78	3.10	4.10	28.41	33.16	11.82	10.41
Fe_2O_3	0.00	0.00	0.00	0.00	0.00	0.00	0.00	0.00	0.00	0.00	0.00	0.00	0.00	0.00	0.00	0.00	0.00	0.00
CuO	0.58	0.40	0.21	0.22	0.10	0.05	1.80	1.85	0.54	0.81	1.94	6.12	6.40	5.52	10.78	2.19	24.06	25.81
Total	74.48	78.85	82.12	81.76	62.72	63.84	85.18	82.06	68.04	64.15	87.51	89.83	83.43	83.42	86.59	84.59	84.18	85.02
Structural formulaes based on 11 oxygen atoms for smectite and I/S, 25 oxygen atoms for corrensite-type and 14 oxygen atoms for chlorite																		
Na	0.04	0.04	0.12	0.11	0.04	0.04	0.15	0.15	0.19	0.11	0.00	0.00	0.00	0.00	0.04	0.03	0.04	0.04
Mg	0.36	0.35	0.29	0.29	0.30	0.30	3.00	3.21	3.34	3.34	1.98	1.77	1.63	1.85	0.90	1.14	0.75	0.77
Al	1.69	1.71	1.95	1.95	1.49	1.51	3.71	3.79	3.55	3.53	2.41	2.20	1.98	2.03	1.94	2.11	1.97	1.95
Si	3.85	3.77	3.59	3.58	3.69	3.74	7.23	7.05	6.93	6.96	3.28	3.30	3.24	3.16	3.18	3.01	3.34	3.34
K	0.12	0.26	0.32	0.33	0.58	0.49	0.14	0.15	0.29	0.21	0.02	0.03	0.11	0.09	0.00	0.00	0.00	0.00
Ca	0.14	0.11	0.05	0.05	0.06	0.06	0.06	0.07	0.06	0.11	0.01	0.03	0.03	0.03	0.01	0.01	0.02	0.02
Ti	0.00	0.00	0.00	0.01	0.00	0.01	0.01	0.01	0.02	0.00	0.00	0.00	0.00	0.00	0.00	0.00	0.00	0.00
V	0.02	0.07	0.13	0.13	0.38	0.31	0.33	0.30	0.01	0.00	1.00	1.07	1.36	1.26	0.00	0.05	0.15	0.16
Mn	0.00	0.00	0.00	0.00	0.00	0.01	0.02	0.00	0.02	0.02	0.00	0.00	0.00	0.01	0.08	0.10	0.02	0.01
Fe^{2+}	0.11	0.17	0.12	0.13	0.15	0.15	1.02	1.06	2.02	1.99	0.17	0.22	0.27	0.36	2.78	3.26	1.18	1.03
Fe^{3+}	0.00	0.00	0.00	0.00	0.00	0.00	0.00	0.00	0.00	0.00	0.00	0.00	0.00	0.00	0.00	0.00	0.00	0.00
Cu	0.04	0.02	0.01	0.01	0.01	0.00	0.23	0.25	0.09	0.15	0.14	0.44	0.51	0.44	0.95	0.19	2.17	2.30
Ch int	0.45	0.52	0.55	0.53	0.73	0.65	0.41	0.44	0.60	0.55	n.d.	n.d.	n.d.	n.d.	n.d.	n.d.	n.d.	n.d.
oct	2.07	2.08	2.09	2.10	2.01	2.02	7.54	7.67	7.98	8.00	4.99	5.01	5.00	5.12	5.82	5.87	5.56	5.57

tri-trioctahedral chlorite (near 6 cations for 14 oxygens) essentially composed 2.8–3.3 atoms per formula unit (a.p.f.u) of Fe^{2+}, Al 1.10–1.20 a.p.f.u., Mg 0.95–1.15 a.p.f.u. and Cu 0.2–0.95 a.p.f.u. (2–25.8 wt.% CuO). V_2O_3 concentration of these chlorites vary from none to about 1.7 wt.%. Regarding the relatively low octahedral occupancy in the structural formulas of chlorite which contain the highest V_2O_3 amounts (Table 2) it cannot be excluded that these analyses result of mixture of Cu-rich tri-trioctahedral chlorite with V(Cu)- rich di-trioctahedral chlorite.

5.4. Bulk rock geochemistry

Bulk chemical composition of sandstones belonging to different parts of the redox system shows variations in oxides and trace elements (Table 1). In order to understand the behavior of oxides in the redox system, the chemical compositions of altered/mineralized sandstones are compared with the unaltered rocks (red sandstone). Calcite cementation is a common pore filling mineral in all diagenetic facies. In order to interpret chemical variations without calcite influence, major oxides were normalized to 100% after calcite extraction and illustrated in Harker-type diagrams with SiO_2, FeO, MgO, Fe_2O_3, Na_2O, TiO_2, V, Cu and U plotted against Al_2O_3 (Fig. 11).

The REE show a constant pattern independently of the type of sandstone with two outliers, a Cu-bearing sandstone enriched in heavy REE and a white sandstone enriched in medium and heavy REE (Fig. 12; Table 1). The REE distribution of all type of sandstones analyzed are parallel to the REE pattern of the upper continental crust (Fig. 12) with a general decrease from the LREE to the HREE, including the negative Eu-anomaly (McLennan, 1989).

The white sandstone presents higher SiO_2 but lower Al_2O_3, Fe_2O_3, Na_2O and TiO_2 values than the red sandstone being the other oxides, LOI and Cu, V and U in similar concentrations. The MnO enrichment exhibited by some samples of the white sandstone correlates with the enrichment in CaO before calcite extraction.

In the brown sandstone analyzed oxides behave as in the white sandstone but plot close to the field of the gray sandstone. That means the brown facies presents intermediate compositions between gray and white sandstones. The main difference consists on the MgO values which are higher than in the gray and white sandstones.

In the gray sandstone all major and minor oxides, LOI values and Cu-U concentrations behave as in the red sandstone, but the concentration of V is considerably higher than in the red facies.

Two sets of the Cu-ore sandstone were analyzed. The first includes the sandstone rich in Cu-chlorite, which occurs at the white sandstone and redox front interface. This sandstone contains also abundant Cu ore minerals such as malachite, brochantite, chrysocolla, chalcocite and iron minerals like pyrite and Fe-oxides. When compared with the red sandstone higher FeO, MgO, Fe_2O_3, LOI, U, V and Cu, and lower Na_2O, TiO_2, Al_2O_3 and SiO_2 concentrations are observed. The second set of Cu-ore sandstone analyzed corresponds to a sandstone with Cu ore widespread in the white sandstone far from the redox front which do not contain Cu-chlorite. It presents almost the same geochemical behavior than Cu-chlorite rich sandstone (higher Fe_2O_3, LOI, Cu and U and lower Al_2O_3, SiO_2 and Na_2O), but with FeO and MgO concentrations similar than those in the red sandstone.

6. Discussion

In the study area, widespread alteration and associated Cu-V mineralization of the sedimentary rocks indicate that large amounts of extra-formational fluids circulated. Changes in color of sandstones from the Huincul Formation is based on authigenic minerals and not in detrital provenance variations. This assumption is supported by the homogeneous modal composition and

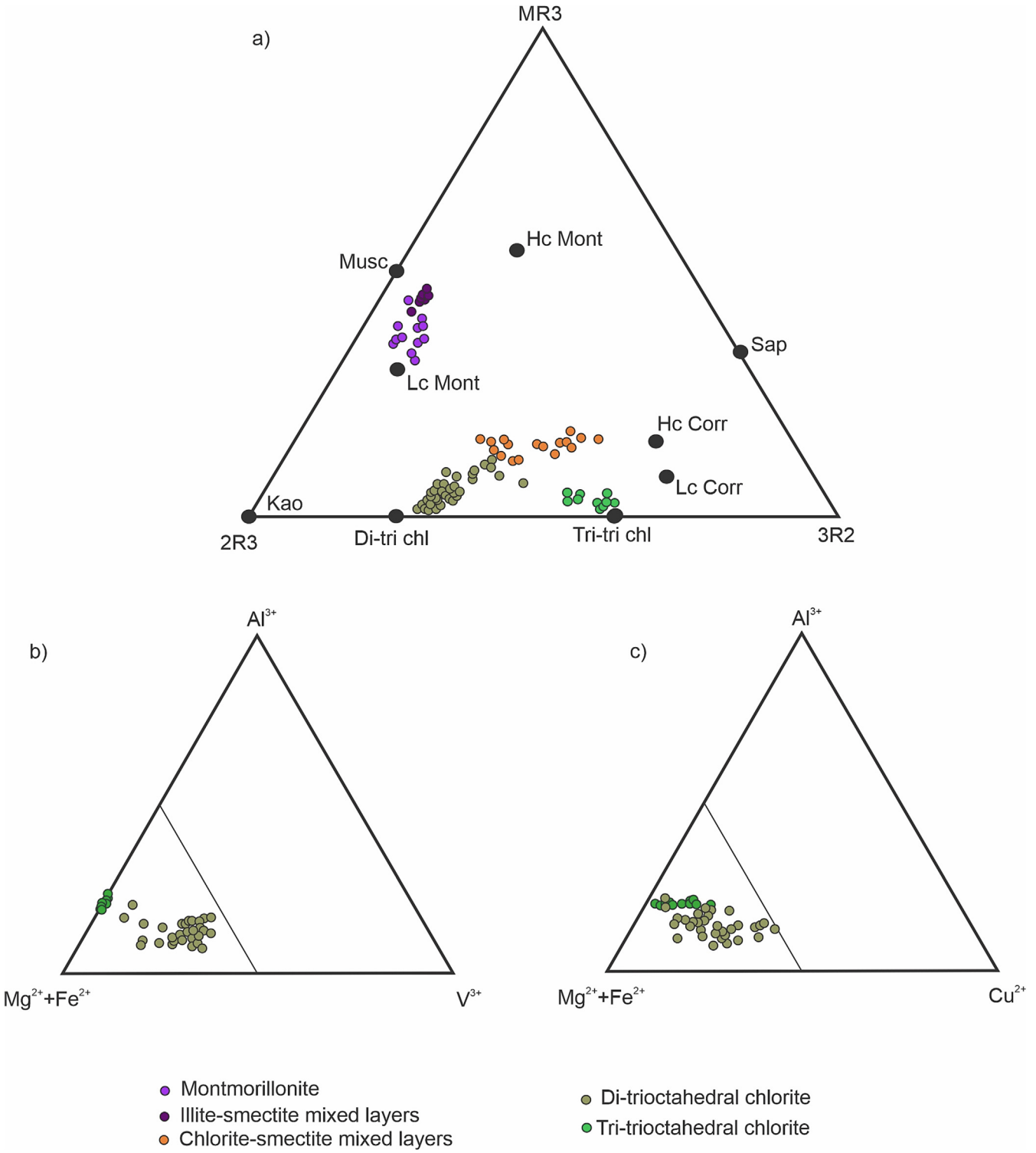


Fig. 10. Microchemical characterization of clay minerals. (a) Plot of the clay-mineral composition in the MR_3-$2R^3$-$3R^2$ triangle in which silica is considered as a component in excess, MR^3 = Na + K + 2Ca; $2R^3$ = ((Al + Fe^{3+}) - MR^3)/2, and $3R^2$ = (Mg + Mn + Fe^{2+})/3 (after Velde, 1985). Smectite plot in the field of the montmorillonite, illite–smectite mixed-layers plot between the field of the montmorillonite and muscovite, corrensite-type plot between montmorillonite and chlorite fields and finally V-chlorite plot in the field of di-trioctahedral chlorite whereas Cu-chlorite plot in the field of tri-trioctahedral chlorite. (b,c) Mg + Fe-Al^{3+}-V^{3+} and Mg + Fe-Al^{3+}-Cu^{2+} diagrams where it is possible to observe the presence of divalent (Mg, Fe and Cu) and trivalent (V) cations in di-trioctahedral whereas only divalent cations (Mg, Fe and Cu) occur in tri-trioctahedral chlorite.

REE contents and distribution (Fig. 12), which indicate a unique sediment source with a characteristic geochemical signature (Fralick, 2003; Rainoldi et al., 2014). Constant patterns of the REE indicate that the general type of igneous rock dominant in the detritus comes from the continental crust and is the same in all diagenetic facies (Fralick 2003). Reddening of the sandstone took place during early diagenesis, when infiltration of meteoric water promoted precipitation of grain coating hematite (Brown, 2005) and kaolinite, and with increasing burial, quartz and albite overgrowths and calcite cementation. The reactivation and

Table 3
Chemical composition of diagenetic minerals from Los Chihuidos deposit.

	Brown sandstone											Gray sandstone					
	V-Hem				Bitumen							Mn-Min	Ti-Magnetite			V-Hem	
wt.%	SS16-1	SS16-2	SS16-3	SS16-4	SS16-7	SS16-8	SS16-9	SS16-10	SS16-11	SS16-12	SS16-13	SS16-18	SS7-1	SS7-2	SS7-3	SS7-4	SS7-5
Na_2O	0.52	0.12	0.25	0.22	0.37	0.50	0.64	0.47	0.68	0.64	0.54	0.54	0.23	0.26	0.96	0.25	0.22
MgO	1.91	0.17	0.88	0.43	0.42	0.38	0.35	0.35	0.45	0.37	0.36	4.56	1.51	1.18	0.92	0.61	0.33
Al_2O_3	10.82	2.13	9.51	3.45	1.73	1.87	2.13	2.07	2.40	1.72	1.25	4.73	0.42	1.42	3.65	1.66	1.33
SiO_2	6.35	8.64	4.58	7.04	2.58	2.20	2.47	2.83	5.18	2.25	1.40	2.72	0.58	0.23	9.67	3.42	0.54
K_2O	0.08	0.08	0.04	0.00	0.05	0.12	0.13	0.14	0.21	0.10	0.02	0.19	0.06	0.00	0.04	0.37	0.00
CaO	0.58	0.75	0.46	0.66	1.20	0.97	1.26	1.11	1.32	1.23	0.69	0.78	0.10	0.02	0.12	0.02	0.00
TiO_2	0.00	0.11	0.07	0.00	0.18	0.38	0.45	0.48	0.46	0.43	0.39	0.19	5.19	16.52	11.85	2.48	1.76
V_2O_3	1.23	0.41	2.42	0.76	0.68	0.36	0.50	0.48	0.37	0.26	0.86	0.00	0.00	0.00	0.00	9.01	1.31
MnO	1.50	0.15	1.55	1.17	5.71	7.85	9.72	9.71	10.29	9.92	6.25	37.73	0.42	0.21	0.01	0.14	0.21
FeO	0.00	0.00	0.00	0.00	2.70	2.48	3.15	3.15	3.12	2.80	1.47	0.00	0.00	0.00	0.00	0.00	0.00
Fe_2O_3	52.89	76.04	58.29	60.05	0.00	0.00	0.00	0.00	0.00	0.00	0.00	2.50	82.49	73.89	65.90	75.46	89.61
CuO	4.57	3.73	4.73	6.62	7.53	13.49	13.62	9.06	9.74	10.06	17.00	6.38	0.00	0.00	0.00	0.00	0.00
S	n.a.	n.a.	n.a.	n.a.	0.72	1.22	0.59	0.53	0.62	0.44	0.81	n.a.	n.a.	n.a.	n.a.	n.a.	n.a.
Cl	n.a.	n.a.	n.a.	n.a.	3.51	3.86	2.93	1.90	1.86	2.29	3.22	n.a.	n.a.	n.a.	n.a.	n.a.	n.a.
Total	79.93	80.88	71.56	72.86	27.39	35.69	37.95	32.28	36.72	32.50	34.25	53.95	91.00	93.74	93.13	93.41	95.32

n.a.: not analyzed.

development of basement faults and gas chimneys during the Andean orogeny (Cevallos et al., 2014) resulted in the upflow of hydrocarbon-bearing fluids up to the permeable red beds of the Huincul Formation, which were sealed by the shales of the Cerro Lisandro Formation. The incoming of hydrocarbons in the oxidized red beds developed a redox system where most cements including hematite were dissolved, iron was reduced, leached and transported by solutions, promoting the bleaching of the previous red sandstone (Rainoldi et al., 2014, 2015; Pons et al., 2015, Pons et al., 2017, Pons et al., 2021); only minor reduced iron was precipitated as pyrite (Rainoldi et al., 2019). Redox reactions resulted in hydrocarbons oxidation and the precipitation of calcite in the white sandstone (Rainoldi et al., 2014). At the redox front, distinctive Eh-pH conditions promoted the precipitation of V, mainly as vanadium-bearing clay minerals (Rainoldi et al., 2014, 2019). Microthermometry of fluid inclusions hosted in calcite of the white sandstone indicates warm (av. 95 °C) fluids with salinities between 5.3 eq. wt.% NaCl and 0.4 eq. wt.% NaCl, suggesting the involvement of oil field brines and low-salinity waters expelled from clays (Rainoldi et al., 2019) during V mineralization. The occurrence of V has been observed worldwide in oil fields and hydrocarbon source rocks (Breit and Wanty, 1991; Parnell and Carey, 1995). In the hydrocarbon source rocks, under reducing conditions, vanadium is reduced from V^{5+} to V^{4+}, which could be removed by surface adsorption processes or by organometallic ligands (Emerson and Huested, 1991; Wanty and Goldhaber, 1992; Morford and Emerson 1999). Under more strongly reducing conditions, by reaction with H_2S (Wanty, 1986) or possibly through reaction with residual organic matter, V^{4+} is further reduced to V^{3+} and can be taken up by porphyrins (Breit and Wanty, 1991). In most cases, sedimentary V mineralization is associated with U (e.g. Whitney and Northrop, 1986).

In the Neuquén Basin, V has been identified through chemical analysis of the source rocks from the Vaca Muerta Formation (Spalletti et al., 2014; Hernández Bilbao, 2016), and in bitumen infill of veins (asphaltites) from the La Escondida deposit located 60 km east of Los Chihuidos deposit, yielding up to 0.2 % V (Parnell and Carey, 1995). Hydrocarbons originated in the source rocks migrated towards the permeable fluvial sandstones of the Huincul Formation and were able to transport these V-rich organic compounds transported by organic complexes (Algeo and Maynard, 2004). The Los Chihuidos Cu–V redox front differs considerably if compared with the typical roll front U-deposits, as a consequence of fluids hydrodynamics at a regional scale. U-roll front deposits form at the redox front between incoming U-bearing oxidizing and hosting reducing regional aquifers (Cuney and Kyser, 2009 and references therein; Bonnetti et al., 2015; Jin et al., 2020). At Los Chihuidos, the redox front develops at the contact between the invading reducing waters and the oxidizing regional aquifer (Fig. 6). This strongly limits the ability to transport uranium up to the redox fronts because the solubility of U (U^{4+}) is extremely low in reducing waters (Langmuir, 1978). Thus, significant amounts of U could not be transported by the hydrocarbon-bearing solutions to concentrate this element at the developed redox front. In this scenario, a unique and singular type of redox system at the Los Chihuidos Cu-V deposit is developed, in which the main mineralogical and geochemical characteristics are the result of three stages of distinctive geochemical fluid flow.

6.1. Stage 1: Hypogene vanadium ore

The Los Chihuidos block uplift during the Late Oligocene–Miocene (Zamora Valcarce et al., 2009) fostered the influx of hydrocarbons into the red beds of the Neuquén Group (Cevallos et al., 2014), carrying V (Cu)-organic complexes, which resulted in the establishment of a redox system with hypogene V (Cu) mineralization. Change in Eh-pH conditions at the redox front may have favored the destabilization of the soluble complexes generated during bleaching of the sandstone. Dissolution of detrital and diagenetic minerals (feldspars, lithic fragments and kaolinite) provided Al, Fe, Mg, Na, K and Si for the V- and Cu-rich clay minerals with V-bearing hematite which crystallized next to the redox front. Vanadium-rich montmorillonite, illite–smectite mixed-layer minerals and hematite in the gray sandstone represent more oxidizing conditions. Montmorillonite is a dioctahedral clay mineral that may incorporate V^{3+} in the octahedral position. Upon smectite recrystallization, V was further incorporated into localized illite–smectite mixed-layer minerals. Incorporation of V into clay mixed-layer minerals during the smectite illitization by interaction with extraformational V-rich fluids have been identified in other sediment-hosted V deposits (Northrop et al., 1990; Peacor et al., 2000; Lewis et al., 2010). A vanadium clay mineral with its composition intermediate between smectite and illite has been also identified in asphaltite deposits from the Vaca Muerta Formation at the Buta Ranquil mine (Parnell and Carey, 1995).

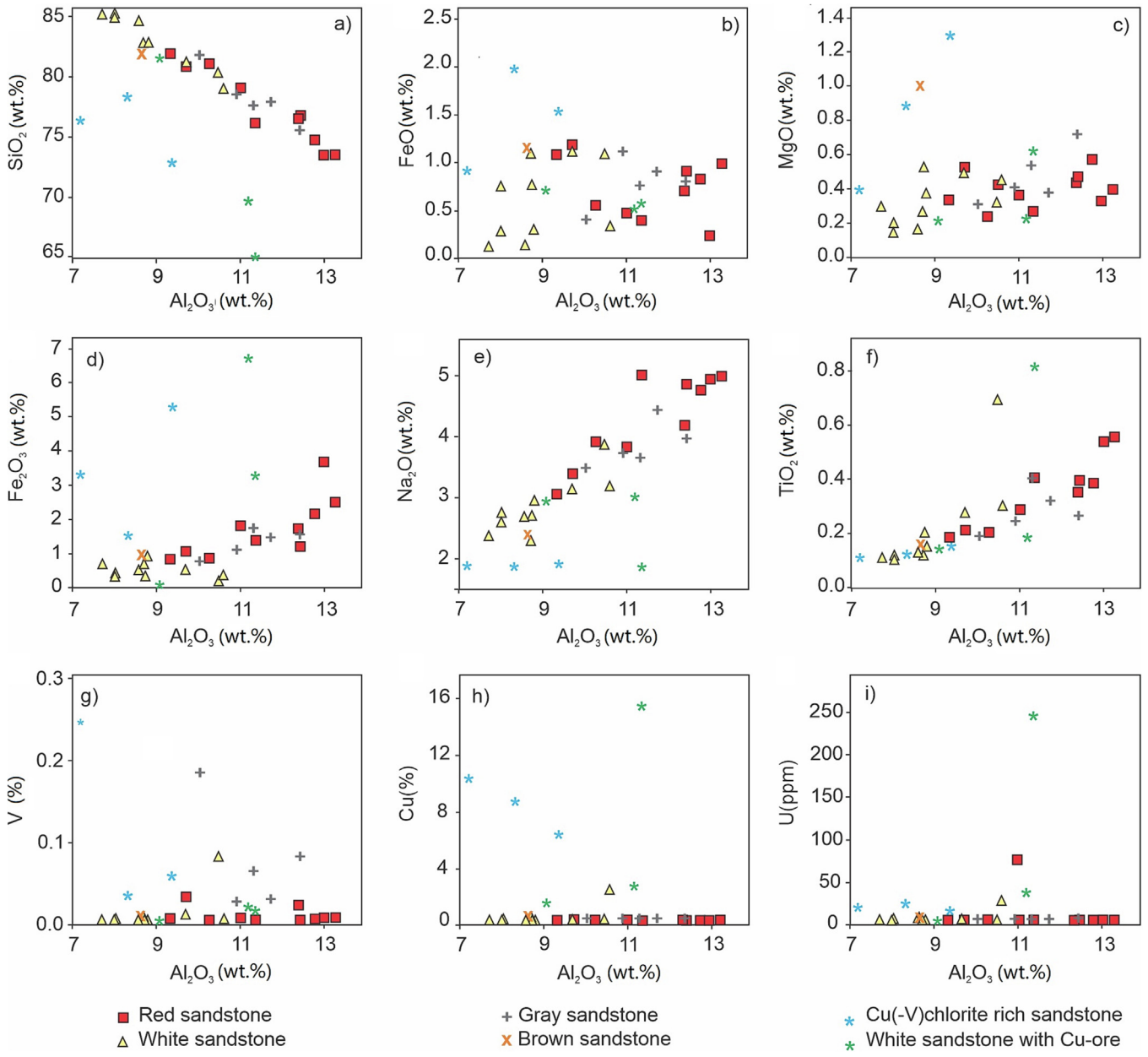


Fig. 11. Harker-type diagrams showing the major, minor and trace element variations of red, white, gray, brown, and Cu mineralized sandstones. (For interpretation of the references to color in this figure legend, the reader is referred to the web version of this article.)

Several studies have shown that in low-to moderate-temperature geological systems, corrensite-type minerals may crystallize as a discrete mineral phase prone to be converted subsequently into chlorite through chlorite-corrensite mixed-layer series (Beaufort et al., 1997, 2015; Murakami et al., 1999; Drits et al., 2011). The corrensite-type minerals observed in the gray and brown sandstones, which represent the external part of the redox front (next to the unaltered red sandstone) at Los Chihuidos, are assumed to be formed under reducing conditions and neutral to slightly basic pH conditions. In the same way, the di-trioctahedral V (Cu) -rich chlorite observed in the dark greenish gray sandstone could have resulted from the complete chloritization of corrensite-type minerals towards the inner part of the redox front in which stronger reducing conditions and high concentrations of V and Cu prevailed in solutions (Fig. 6). This di-trioctahedral V(Cu)-rich chlorite is characteristic of the main V ore stage at Los Chihuidos deposit (Figs. 6 and 10b). The chloritization could have been developed during the migration of the redox interface, where reducing fluids moved down dip into the reservoir, overlapping the previous redox interface with Cu-V corrensite-type, promoting the chloritization process and continuous upgrading of the V-Cu anomalies with V-rich chlorite at the redox front and Cu-rich chlorite at the redox interface (contact between the redox front and the reducing compartment i.e. white sandstone; Fig. 6b). This mechanism has been explained in U roll front systems where translation stage of the redox front promotes dissolution and reprecipitation of Fe-sulfides with increasing metal content (Bonetti et al., 2020). Vanadium-bearing chlorite or chlorite-corrensite mixed-layer minerals have been reported to be indicative of the redox fronts in the V-U deposits of the Henry Basin, Utah, in the United States (Northrop et al., 1990). The high amount of Fe and Mg-rich detrital volcanic fragments and the presence of $MgCl_2$ in diagenetic fluids related to bleaching based on fluid inclusions analysis (Rainoldi et al., 2019), indicate that the

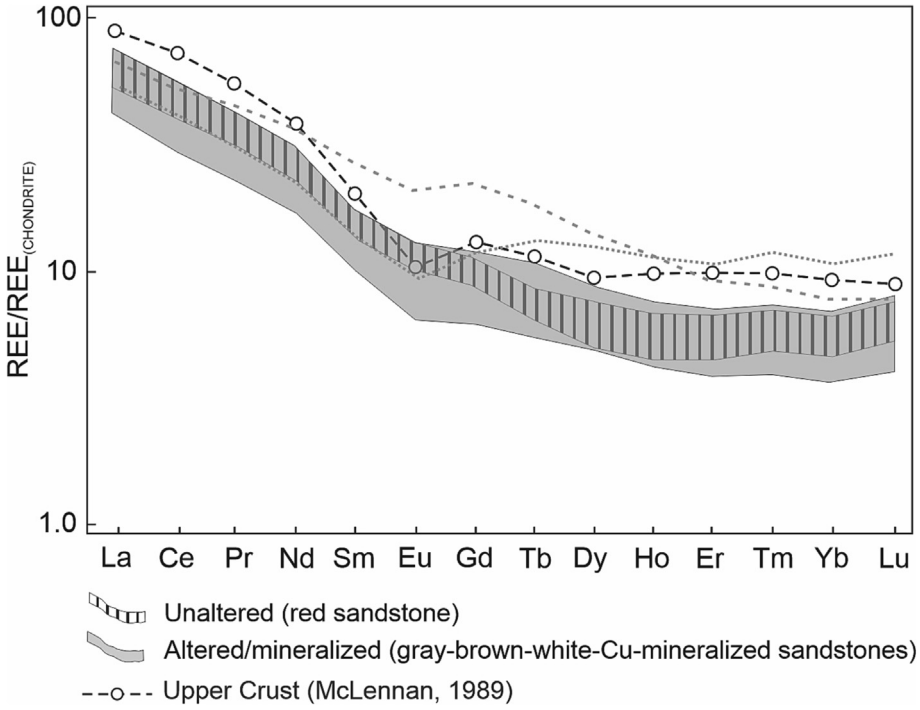


Fig. 12. Whole rock REE concentrations normalized to average chondrite (Boynton, 1984) for the analyzed sandstones (n = 30) showing a similar REE pattern of the upper continental crust (McLennan, 1989). The dotted and striped patterns correspond to a Cu-mineralized and white sandstones (n = 2) enriched in M−REE and H-REE.

prevalence of Mg and Fe cations favored the chloritization over the illitization process.

The fact that V and Cu were detected together in almost all the clay minerals species found within and close to the redox front indicate that both metals were in the resident solution at the moment of the clay crystallization. Late incorporation of Cu in V-rich clay minerals is difficult to assume because the only mechanism for introduction of Cu in a V-rich clay material would be dissolution-crystallization. As there is no petrographic evidence of the alteration and subsequent replacement of earlier V-bearing clay minerals by Cu-bearing ones, it is then concluded that both V and Cu were in solution during the crystallization of the clay minerals sequence. Bulk rock chemical analysis of the Vaca Muerta source rock indicate considerable amounts of V (average 246 ppm) and minor Cu contents (average 35 ppm) (Spalletti et al., 2014); geochemical analyses of the unaltered red beds also indicate concentrations of Cu between 10 ppm and 260 ppm (Table 1). In this context, minor amounts of Cu could have travelled together with V in the hydrocarbon-bearing solutions or could have been leached from the red bed strata (Pons et al., 2017), precipitating as secondary metal in the clay minerals species at the redox front. Vanadium is found essentially as a substitute for Al in the clay minerals which contain dioctahedral layers (i.e., smectite, illite–smectite mixed-layer minerals, Al-rich corrensite-type mineral and di-trioctahedral chlorite) while Cu is found as a substitute for Fe^{2+} or Mg into clay minerals which contain trioctahedral sheets (corrensite-type and both di-tri and tri-trioctahedral chlorite). This explains the lacks of V in the tri-trioctahedral Cu-chlorite.

Considering that all diagenetic facies (red, white, brown, gray and greenish gray sandstones) present the same modal composition and same REE pattern, it is interpreted that major oxides trends (Fig. 11) are due to postdepositional processes. When comparing unaltered (red) with altered/mineralized (white, brown, gray and greenish gray) sandstones, the most remarkable difference is the partial dissolution of diagenetic kaolinite, detrital plagioclase and volcanic lithic grains (predominantly basic and mesosilicic compositions) in the latter. Dissolution of diagenetic minerals and detrital clasts is directly reflected in the maximum average porosity of diagenetic facies, increasing from red (12.5%) to brown (17.5%), gray (19%) and white (24%) sandstones (Rainoldi et al., 2014). Therefore, mineral dissolution exceeded the volume of new formed minerals, indicating large-scale element transport (Milliken et al., 1994; Wilkinson et al., 2003). Hydrocarbons influx into the red sandstone were accompanied with formation waters and other organic and inorganic species in a water-wet system (i.e., organic acids, methane, and CO_2; Carothers and Kharaka 1978). Organic acids, in particular, may have promoted the strong dissolution of aluminosilicates and carbonates but only minor dissolution of quartz and preservation of diagenetic albite (Rainoldi et al., 2014). As a consequence of the partial dissolution of diagenetic kaolinite, detrital plagioclase and volcanic lithic grains in the reduced white facies, the contents of Al_2O_3, Na_2O and TiO_2 are lower than in the red sandstone. Petrography evidences minor mobility of Ti at local scale, where this element was released from Ti-magnetite (Fig. 7d) and precipitated on authigenic anatase (Fig. 7b); however, Ti concentrations indicate that during bleaching Ti transport at large-scale also occurred. Mobility of Al and Ti, two highly immobile elements, can be attributed to the presence of organic acids, which can form chelation complexes with Al^{3+} and Ti^{4+} (Surdam et al., 1984, Surdam et al., 1989; Salmien et al., 2005). Transport of Al in hydrocarbons reservoirs due to complexing by organic compounds (Maliva et al., 1999) and in sandstone-shale succession as a result of clay authigenesis (Milliken et al., 1994; Wilkinson et al., 2003) has been determined despite the common assumption of Al immobility. Lower concentrations of Al in the bleached sandstone as a consequence of dissolution of aluminosilicates due to organic acids effect have been previously documented in the SSC deposits of the Neuquén Basin (Rainoldi et al., 2014; Pons et al., 2017) and worldwide (MacIntyre et al., 2023). Other plausible explanation could be the precipitation of a silica-rich phase in the white sandstone, resulting in higher SiO_2 and apparent depletion of Al_2O_3, Na_2O and TiO_2. The

oxide trend is explained as decrease of Al, Na and Ti due to clasts dissolution and elements outflow since (i) minerals precipitated in the white sandstone are not siliceous (calcite and pyrite) except for minor smectite, (ii) detrital aluminosilicates are strongly dissolved but quartz is slightly affected, (iii) detrital titanomagnetite is dissolved and replaced by V-hematite (Fig. 7d) and (iv) strong clast dissolution is reflected in a notable increase in sandstone porosity, and (v) porosity development through mineral dissolution requires export of major-element constituents to be preserved (Wilkinson et al., 2003).

Ferric iron oxide is depleted in the white sandstone due to the absence of hematite coatings typical of the red bed. Potassium sourced by detrital K-feldspar dissolution was incorporated in the clay minerals. Simulations in oil-filled reservoirs have demonstrated that oil emplacement limit K mobility and maximized illite formation, preventing K diffusion and migration (Thyne et al., 2001). As K-feldspar is a minor component in the Huincul Formation, the K released was reprecipitated in smectite and illite–smectite mixed-layers instead of illite. The MgO and FeO were released from detrital volcanic fragments after clasts dissolution and incorporated in clay minerals. The MnO enrichment exhibited by some samples of the white sandstone correlates with the enrichment in CaO before calcite extraction, suggesting the presence of MnO in the calcite cement, as observed in other altered white sandstones in the Neuquén Basin (Pons et al., 2015).

At the redox front, due to the precipitation of abundant V-rich diagenetic minerals (montmorillonite ± illite–smectite, corrensite-type, chlorite, hematite) the concentrations of major oxides were preserved and particularly enrichment of V occurred (Fig. 11), as observed in other sandstone-hosted U-V deposits (Schmid et al., 2020). Metastable conditions at the redox front may have favored the coexistence of Fe^{3+} and Fe^{2+}. In the gray sandstone, under more oxidizing conditions Fe^{2+} was incorporated in montmorillonite and Fe^{3+} was incorporated in hematite. In the dark greenish gray and brown sandstones, under more localized reducing conditions, Fe^{2+} was incorporated in corrensite-type and V-chlorite, which are both Mg and Fe-rich. The gray sandstone also lacks hematite coatings but preserves the Fe_2O_3 content due to the precipitation of secondary V-hematite; only minor secondary hematite has been detected in the brown sandstone, resulting in lower Fe_2O_3 concentrations, as observed in other SSC deposits (Pons et al., 2017). The FeO, MgO and MnO enrichment exhibited by the Cu-chlorite mineralized sandstone (Fig. 11b, c, i) at the redox interface may be related to the predominance of tri-trioctahedral chlorite.

Manganese has been identified in the brown sandstone occurring in bitumen impregnations (5.7–13.7 wt.% MnO), in secondary hematite (0.15–1.5 wt.% MnO), and as local occurrence of an undetermined MnO (37.7 wt.% MnO) around corrensite-type mineral (Fig. 7e). In the gray sandstone, only secondary hematite contains MnO with values up to 0.21 wt.% (Table 3), suggesting that Mn was mainly precipitated in the more reducing portions of the system. However, Mn-bearing minerals are in very low amounts.

Calcite is a common diagenetic mineral in the white sandstone (Rainoldi et al., 2019) but is absent in the hypogene and supergene V ore, which is recorded by the low concentrations of CaO in the bulk-rock analysis (Table 1). The precipitation of clay minerals in the V ore localized at the redox front, which are scarce in the white sandstone, may have promoted the decrease of the pH by the removal of hydroxide ions from solution to form $V(OH)_3$, $Fe(OH)_2$ and $Mg(OH)_2$ at the octahedral sites of clay minerals, preventing calcite precipitation (Northrop et al., 1990).

The spatial transition of V and/or Cu bearing clay minerals observed through the mineralized redox fronts at Los Chihuidos deposit (kaolinite → smectite → illite/smectite → corrensite-type → di-trioctahedral chlorite → tri-trioctahedral chlorite) and the related variation of V-Cu concentrations in bulk rock are indicative of increasing pH and decreasing Eh of resident solutions from red to white sandstones during the hypogene mineralization process (Fig. 6).

6.2. Stage 2: hypogene copper ore

Later stages of Los Chihuidos block uplift during Middle/Late Miocene (Zamora Valcarce et al., 2009), may have promoted the reactivation of the structures and upflow of metal-charged basinal brines into the Huincul Formation, resulting in main stage of Cu mineralization. This episode is characterized by the precipitation of chalcocite and djurleite in contact with hydrocarbons in the white sandstone which was acting as hydrocarbon reservoir or carrier bed (Rainoldi et al., 2019), and also at the inner part of the redox front where Cu-chlorite was previously precipitated. The presence of main Cu mineralization subsequent to V-bitumen emplacement has been observed in asphaltite veins in the Neuquén province (Parnell and Carey, 1995).

Fluid inclusions hosted in calcite associated with Cu-sulfides indicate that two types of fluids were present at the time of Cu-ore formation, a warm and low-salinity parental fluid and an incoming lower temperature ~80 °C and higher salinity (>16.6 wt.% NaCl equiv.) brine that could have carried Cu and sulfate. Besides, negative $\delta^{34}S$ values (−45.2‰ to − 41.7‰) of sulfides and extremely large isotopic fractionation (−59‰ to −64‰) suggest infiltration of meteoric waters which may have resulted in bacterial sulfate reduction and precipitation of chalcocite-djurleite (Rainoldi et al., 2019).

Copper mineralized sandstones show the lowest concentrations of SiO_2, Al_2O_3, Na_2O and CaO, pointing to strong silicates dissolution and/or (Cu–V) mineral precipitation including sulfides, sulfates and carbonates which contribute to an apparent depletion of the major oxides and is reflected in the highest LOI values.

6.3. Stage 3: supergene vanadium ore

During the Andean uplift, infiltration of meteoric water promoted chemical reactions with the hypogene mineralization. In the gray sandstone localized in the oxidizing portion of the redox front, V (Cu) montmorillonite and hematite remained stable during meteorization, preserving their mineralogy during uplift. In the most reducing portion of the redox system, V and Cu held within the chlorite fraction were remobilized during weathering and became part of the new mineral facies. In the dark greenish gray sandstone, vanadates like volborthite, vésigniéite and gamagarite (Fig. 7l) and uranovanadates (francevillite) precipitated; this mineral association was also identified in other SSC deposit of the Neuquén Basin, e.g. Barda González and Tordillos (Pons et al., 2009, Pons et al., 2017). In the Cu-bearing sandstone with relatively high pyrite content, oxidation resulted in the liberation of Fe and its association with V and Cu remobilized from the clay and sulfide fractions and precipitation of Cu-Fe-V oxides (Fig. 7k–n), evidenced in the whole rock chemistry by the highest Fe_2O_3 content (Fig. 11d). Incorporation of V in oxides during meteorization has been observed in shale-hosted deposits, with the V oxides as the main ore mineral (Lewis et al., 2010); partial replacement of Fe for V in oxides has also been observed in other sandstone-hosted uranium-vanadium deposits (Schmid et al., 2020). The hypogene Cu-ore was also oxidized, resulting in Cu oxides (cuprite), carbonates (malachite and azurite) and silicates (chrysocolla) (Fig. 7h–o). Oxidizing fluids also promoted the mobilization of other minor metals such as U, which were incorporated with V in the uranovanadate "francevillite", resulting in higher U concentrations (Fig. 11l).

Vanadium mineralization at Los Chihuidos SSC deposit shows similarities with the sandstone-hosted vanadium-uranium deposits of Utah (Whitney and Northrop, 1986; Northrop et al., 1990; Meunier, 1994), the main producer of vanadium from sandstone-hosted deposits on a global scale (Kelley et al., 2017), with mineralization occurring as vanadium-bearing clay minerals. The presence of di-trioctahedral chlorite as main vanadium ore mineral evidences the crystallization of this specific clay mineral phase during vanadium precipitation and ore upgrade. In the Henry Basin (Utah) deposits, vanadium-uranium minerals formed in intrabasinal synclines where the redox boundary, related to the brine-meteoric water interface, intersected sandstone horizons containing anomalous concentrations of organic matter. Multiple ore horizons, and the observed complexities of these intervals, were explained as the result of upward migration of the brine-meteoric water interface with continued compaction and tectonic activity. (Northrop et al., 1990).

In the Neuquén Basin, SSC deposits occur in red bed sequences bleached due to hydrocarbon circulation and establishment of a redox system marked by colorful variation of diagenetic facies (Pons et al., 2009, 2014, 2015, 2017, 2021; Rainoldi et al., 2014, 2015, 2019). At the Tordillos SSC deposit, unaltered red rocks are only preserved as lenticular reddish-brown siltstone whereas most permeable paleochannels were pervasively bleached; as a result, local redox fronts were identified with V occurring only as a trace element. The development of a regional redox front at the Los Chihuidos deposit allowed the development of continuous upgrading V zones, being its regional configuration a useful guide to explore for similar deposits in poorly explored regions of the basin and similar basins worldwide.

7. Conclusion

Of the numerous sediment-hosted stratiform Cu deposits in the Neuquén Basin, the Los Chihuidos deposit is unique given that it contains the largest reserves of Cu and V as a by-product. The mineralogical and geochemical data presented in this study allows for a new comprehensive understanding of the V mineralization in the Los Chihuidos SSC deposit. The influx of hydrocarbon-rich reducing fluids enriched in V with minor amounts of Cu into the red succession prompted to bleaching of red beds and reached intermediate redox conditions at the boundary zone. The resulted redox front between the red and white beds is characterized by a series of colored sandstones grading from gray to brown and finally dark greenish grey, and in which is observed a sequence of V- and Cu-bearing clay minerals. Vanadium-rich montmorillonite (associated with V-hematite) in the gray sandstone predominates, however, Cu-V corrensite-type and V-rich chlorite in the brown and dark greenish grey sandstones also occur, indicating metastable oxidizing-reducing conditions and enhancing the role of the redox front in the precipitation of V. At the innermost part of the redox front, where the most reducing conditions at the redox interface predominates, the precipitation of a Cu-rich chlorite took place. During the life of the redox system, the translation stage of the redox front promoted chloritization and illitization processes with increasing V and Cu contents and the subsequent ore upgrade. Oxide trends observed are interpreted to be the result of diagenetic phenomenon and not a primary sedimentary feature.

Subsequently, the influx of oxidizing Cu-charged brines in the reducing compartment characterized by the white sandstone, found a redox tramp and precipitated the main copper ore (copper sulfides).

Finally, uplift and exhumation of the system favored downward infiltration of oxidizing meteoric waters in the earlier hypogene mineralized zones, resulting in widespread vanadates, urovanadates and Cu-Fe-V oxides precipitation at the redox front. Copper mineralization localized in the reducing compartment of the system also resulted in supergene Cu minerals with covellite, brochantite, malachite, azurite, chrysocolla and cuprite as the most abundant.

CRediT authorship contribution statement

Ana L. Rainoldi: Conceptualization, Methodology, Investigation, Writing – original draft, Visualization. **Daniel Beaufort:** Methodology, Investigation, Data curation, Funding acquisition. **Marta B. Franchini:** Visualization, Investigation, Funding acquisition, Supervision. **Adolfo Giusiano:** Conceptualization, Resources. **Sabine Petit:** Validation. **Patricia Patrier:** Validation. **M. Josefina Pons:** Writing – review & editing.

Declaration of Competing Interest

The authors declare that they have no known competing financial interests or personal relationships that could have appeared to influence the work reported in this paper.

Acknowledgements

We are grateful to Ariel Testi for his collaboration during fieldwork. The research was supported by European Commission through its Erasmus Mundus Internship program, which allowed ALR to conduct the clay mineral analysis at the IC2MP (Université de Poitiers), FONCyT (PICT No. 2010-2608), CONICET (PIP No. 6043, PIP No. 1083, and PIP No. 330), Universidad Nacional del Comahue (PIP No. 04/I167), Universidad Nacional del Sur (SECyT through its Internship program in Research and PGI 24/H144). The authors also acknowledge financial support from the European Union (ERDF) and Région Nouvelle Aquitaine. We thank the two anonymous reviewers and Associate Editor Prof. Manikyamba for their constructive reviews and helpful suggestions and Editorial Advisor M. Santosh for guiding the evolution of this manuscript.

References

Algeo, T.J., Maynard, J.B., 2004. Trace-element behavior and redox facies in core shales of Upper Pennsylvanian Kansas-type cyclothems. Chem. Geol. 206, 289–318.

Anechine, M., Stahlschmidt, E., del Pino, M., 2002. Evaluación petrofísica de reservorios complejos dentro de la Formación Mulichinco. Yacimiento Sierra Chata. Cuenca Neuquina, in: Proc. V Congreso de Exploración y Desarrollo de Hidrocarburos V, Argentina, CD-ROM, 10 pp (in Spanish).

Ardolino, A., Franchi, M., 1996. Geología y Recursos Naturales del Departamento de Añelo, provincia del Neuquén, República Argentina. Dirección Nacional Del Servicio Geológico, Anales 25, 1–212 (in Spanish).

Bailey, S.W., 1982. Nomenclature for regular interstratifications. Am. Mineral. 67, 394–398.

Beaufort, D., Baronnet, A., Lanson, B., Meunier, A., 1997. Corrensite: a single phase or a mixed layered phyllosilicate of the saponite to-chlorite conversion series? The case study of Sancerre-Couy deep drill hole (France). Am. Mineral. 82, 110–125.

Beaufort, D., Rigault, C., Billon, S., Billault, V., Inoue, A., Inoue, S., Patrier, P., 2015. Chlorite and chloritization processes through mixed layer mineral series in low-temperature geological systems – a review. Clay Miner. 50, 497–523.

Beitler, B., Parry, W.T., Chan, M.A., 2005. Fingerprints of fluid flow: chemical diagenetic history of the Jurassic Navajo Sandstone, southern Utah. J. Sediment. Res. 75, 457–561.

Bonetti, C., Zhou, L., Riegler, T., Brugger, J., Fairclough, M., 2020. Large S isotope and trace element fractionations in pyrite of uranium roll front systems results from internally-driven biogeochemical cycle. Geochim. Coscmochim. Acta 282, 113–132.

Bonnetti, C., Cuney, M., Michels, R., Truche, L., Malartre, F., Liu, X., Yang, J., 2015. The multiple roles of sulfate-reducing bacteria and Fe-Ti oxides in the genesis of the Bayinwula roll front-type uranium deposit, Erlian Basin, NE China. Econ. Geol. 110, 1059–1081.

Boynton, W.V., 1984. Cosmochemistry of the rare earth elements: meteoritic studies. In: Henderson, P. (Ed.), Rare Earth Element Geochemistry. Elsevier, Amsterdam, pp. 63–114.

Breit, G.N., Wanty, R.B., 1991. Vanadium accumulation in carbonaceous rocks: a review of geochemical controls during deposition and diagenesis. Chem. Geol. 91, 83–97.
Brown, A.C., 2005. Refinements for footwall red-bed diagenesis in the sediment hosted stratiform copper deposits model. Econ. Geol. 100, 765–771.
Carothers, W.W., Kharaka, Y.K., 1978. Aliphatic acid anions in oil-field waters: implications for origin of natural gas. AAPG Bull. 62, 2441–2453.
Cazau, L., Uliana, M.A., 1973. El Cretácico superior continental de la Cuenca Neuquina, in: Proc. V Congreso Geológico Argentino, Argentina, 131-163 (in Spanish).
Cevallos, M.F., Giusiano, A.E., Franchini, M., Rainoldi, A.L., Martínez, R.S., Carbone, O. C., Alaimo, A.A., 2014. Evidencias de migración terciaria de hidrocarburos en el Dorso de Los Chihuidos, Cuenca Neuquina, Argentina, in: Proc. IX Congreso de Exploración y Desarrollo de Hidrocarburos, Argentina, 133–154 (in Spanish with English abstract).
Cuney, M., Kyser K., 2009. Sandstone-hosted uranium deposits. In: Cuney, M., Kyser, K. (Eds.), Chapter 9: Recent and not-so-recent developments in uranium deposits and implications for exploration. Mineralogical Association of Canada Short Course Series 39, 257 pp.
Di Giulio, A., Ronchi, A., Sanfilippo, A., Tiepolo, M., Pimentel, M., Ramos, V.A., 2012. Detrital zircon provenance from the Neuquén Basin (south-central Andes): Cretaceous geodynamic evolution and sedimentary response in a retroarc-foreland basin. Geology 40, 559–562.
Drits, V.A., Ivanovskaya, T.A., Sakharov, B.A., Zviagina, B.B., Gor'kova, N.V., Pokrovskaya, E.V., Savichev, A.T., 2011. Mixed-Layer corrensite–chlorites and their formation mechanism in the glauconitic sandstone–clayey rocks (Riphean, Anabar uplift). Lithol. Miner. Resour. 46, 566–593.
Emerson, S.R., Huested, S.S., 1991. Ocean anoxia and the concentrations of molybdenum and vanadium in seawater. Mar. Chem. 34, 177–196.
Folk, R.L., Andrews, P.B., Lewis, D.W., 1970. Detrital sedimentary rock classification and nomenclature for use in New Zealand: New Zealand. J. Geol. Geophysics 13, 937–968.
Fralick, P., 2003. Geochemistry of clastic sedimentary rocks: ratio techniques. In: Lentz, D.R. (Ed.), Geochemistry of sediments and sedimentary rocks: evolutionary considerations to mineral deposit-forming environments: Geological Association of Canada, Geotext 4, 85-103.
Garrido, A.C., 2010. Estratigrafía del Grupo Neuquén, Cretácico Superior de la Cuenca Neuquina (Argentina): nueva propuesta de ordenamiento estratigráfico. Rev. Museo Arg Cienc. Nat. 12, 121–177 (in Spanish with English abstract).
Giusiano, A., Bouhier, E., 2009. Mineralización de Cu en el Grupo Neuquén vinculada a la migración de hidrocarburos. Dorso de los Chihuidos, Neuquén, Argentina. Bol. Inf. Pet., 6-18 (in Spanish with English abstract).
Hansley, P.L., Spirakis, C.S., 1992. Organic matter diagenesis as the key to a unifying theory for the genesis of tabular uranium-vanadium deposits in the Morrison Formation, Colorado Plateau. Econ. Geol. 87, 352–365.
Hernández Bilbao, E., 2016. High-resolution che-mostratigraphy, sequence stratigraphic correlation, porosity and fracture characterization of the Vaca Muerta Formation, Neuquén basin, Argentina. PhD thesis, Colorado School of Mines, p. 195 pp..
Jin, R., Teng, X., Li, X., Si, Q., Wang, W., 2020. Genesis of the sandstone-type uranium deposits along the northern margin of the Ordos Basin. China. Geosci. Front. 11, 215–227.
Kay, S.M., Gorring, M., Ramos, V.A., 2004. Magmatic sources, setting and causes of Eocene to Recent Patagonian plateau magmatism (36°S to 52°S latitude). Rev. Asoc. Geol. Arg. 59, 556–568.
Kelley, K.D., Scott, C.T., Polyak, D.E, Kimball, B.E., 2017. Vanadium, chap. U of In: Schulz, K.J., DeYoung, J.H.Jr., Seal, R.R.II, Bradley, D.C. (Eds.), Critical mineral resources of the United States—Economic and environmental geology and prospects for future supply. U.S. Geological Survey Professional Paper 1802, pp. U1– U36, https://doi.org/10.3133/pp1802U.
Langmuir, D., 1978. Uranium solution-mineral equilibria at low temperatures with alications to sedimentary ore deposits. Geochim. Cosmochim. Acta 42, 547–569.
Leanza, H.A., Zanettini, J.C.M., Rodríguez, M.F., 2011. Mapa Geológico de la Provincia de Neuquén. Servicio Geológico Minero Argentino. Instituto de Geología y Recursos Minerales. Buenos Aires, Argentina (in Spanish with English abstract).
Lewis, S.E., Henderson, R.A., Dickens, G.R., Shields, G.A., Coxhell, S., 2010. The geochemistry of primary and weathered oil shale and coquina across the Julia Creek vanadium deposit (Queensland, Australia). Miner. Deposita 45, 599–620.
MacIntyre, T.J., Hitzman, M.W., Thorson, J.P., 2023. Hydrocarbon-induced bleaching and copper mineralization in the Wingate Sandstone, Paradox Valley, Colorado: Two episodes of fluid migration during the evolution of the Paradox Basin. AAPG Bull. 107, 169–189.
Madejová, J., Balan, E., Petit, S., 2011. Application of vibrational spectroscopy to the characterization of phyllosilicates and other industrial minerals. In: Christidis, G.E. (Ed.), Advances in the Characterization of Industrial Minerals. Notes in Mineralogy 9, pp. 171-226.
Maliva, R.G., Dickson, J.A.D., Fallick, A.E., 1999. Kaolin cements in limestones: potential indicators of organic-rich porewaters during diagenesis. J. Sed. Res. 69, 158–163.
Maretto, H., Pángaro, F., 2005. Edad de formación de algunas de las grandes estructuras del engolfamiento de la Cuenca Neuquina: Actividad tectónica durante la depositación de la Fm. Quintuco in: Proc. VI Congreso de Exploración y Desarrollo de Hidrocarburos, Argentina, CD-ROM, 11 p (in Spanish).
McKelvey, V.E., Strobell, J.D., Slaughter, A.L., 1986. The vanadiferous zone of the Phosphoria Formation in Western Wyoming and Southeastern Idaho. US Geological Survey Professional Paper 1465, 27 pp.
McLennan, S.M., 1989. Rare earth elements in sedimentary rocks: influence of provenance and sedimentary process. Rev. Mineral. 21, 169–200.
Meunier, J.D., 1994. The composition and origin of vanadium-rich clay minerals in Colorado Plateau Jurassic sandstones. Clay Clay Mineral 42 (391–401), 401.
Milliken, K.L., Mack, L.E., Land, L.S., 1994. Elemental mobility in sandstones during burial: whole-rock chemical and isotopic data, Frio formation, south Texas. J. Sed. Res., 788–796
Morford, J.L., Emerson, S., 1999. The geochemistry of redox sensitive trace metals in sediments. Geochim. Cosmochim. Acta 63, 1735–1750.
Mosquera, A., Ramos, V.A., 2006. Intraplate deformation in the Neuquén Embayment. In: Kay, S.M., Ramos, V.A. (Eds.), Evolution of an Andean margin: A tectonic and magmatic view from the Andes to the Neuquén Basin (35°-39°S lat): Geological Society of America Special Paper 407, pp. 97–123.
Murakami, T., Sato, T., Inoue, A., 1999. HRTEM evidence for the process and mechanism of saponite-to-chlorite conversion through corrensite. Am. Mineral. 84, 1080–1087.
Northrop, R., Goldhaber, M.N., Landis, G.P., Unruh, J.W., Reynolds, R.L., Campbell, J. A., Wanty, R.B., Grauch, R.I., Whitney, G., Rye, R.O., 1990. Genesis of the tabular-type vanadium-uranium deposits of the Henry Basin. Utah. Econ. Geol. 85, 215–269.
Oinuma, K., Hayashi, H., 1965. Infrared study of clay minerals. Am. Mineral. 50, 1213–1227.
Orión del Sur SA, 2012. Exploration internal report 2012. Los Chihuidos High SSC prospects, Orión del Sur SA.
Orión del Sur SA, 2008. Exploration internal report 2008. Orión del Sur SA.
Parnell, J., Carey, P.F., 1995. Emplacement of bitumen (asphaltite) veins in the Neuquén Basin, Argentina. AAPG Bull. 79, 1798–1816.
Paz, M., Pons, M.J., Giusiano, A., Ćabana, C., Franchini, M., González, E., Impiccini, A., Rainoldi, A.L., 2016. La relación entre la mineralización de Cu y bitumen en el Prospecto La Cuprosa. Rev. Asoc. Geol. Arg. 73, 563–581 (in Spanish with English abstract).
Peacor, D.R., Coveney Jr., R.M., Zhao, G., 2000. Authigenic illite and organic matter: the principal hosts of vanadium in the Mecca Quarry Shale at Velpen. Indiana. Clay Clay Mineral. 48, 311–316.
Pons, M.J., Franchini, M.B., Giusiano, A., Impiccini, A., Godeas, M., 2009. Alteraciones, mineralización de Cu y bitumen en areniscas Cretácicas del Prospecto Barda González, Neuquén. Argentina. Rev. Asoc. Geol. Arg. 64, 321–333 (in Spanish with English abstract).
Pons, M.J., Franchini, M., Giusiano, A., Maydagán, L., Rainoldi, A.L., 2014. Mineralización de Cu (V-U) en la Formación Huincul, prospecto Tordillos, Cuenca Neuquina. Rev. Asoc. Geol. Arg. 71, 537–552 (in Spanish with English abstract).
Pons, M.J., Rainoldi, A., Franchini, M.B., Beaufort, D., Impiccini, A., Cessartti, N., Giusiano, A., Patrier, P., 2015. Mineralogical signature of hydrocarbon circulation in cretaceous red beds of the Barda González area. Neuquén Basin. AAPG Bull. 99, 525–554. https://doi.org/10.1306/08131413170.
Pons, M.J., Franchini, M., Giusiano, A., Patrier, P., Beaufort, D., Impiccini, A., Rainoldi, A.L., Meinert, L., 2017. Alteration halos in the Tordillos sediment-hosted copper deposit of the Neuquén Basin. Argentina. Ore Geol. Rev. 80, 691–715. https://doi.org/10.1016/j.oregeorev.2016.06.011.
Pons, M.J., Franchini, M., Rainoldi, A.L., Giusiano, A., Cesaretti, N., Montagna, A.O., Herrington, R., 2021. Base metal mobility linked to brine and hydrocarbon migration at the Huincul High in the Neuquén Basin, Argentina: Implications for the formation of sediment-hosted base metal deposits. J. Geochem. Expl. 226,. https://doi.org/10.1016/j.gexplo.2021.106778 106778.
Rainoldi, A.L., Limarino, C.O., Giusiano, A., Bouhier, E., 2012. Análisis estratigráfico de la Formación Huincul (Grupo Neuquén) en el prospecto Sapo Sur (37°47'S-69°27'O), Dorso de los Chihuidos, Neuquén (Abstract), in: Proc. XIII Reunión Argentina de Sedimentología, Argentina, 185-186 (in Spanish).
Rainoldi, A.L., Franchini, M., Beaufort, D., Impiccini, A., Giusiano, A., Pons, M.J., Patrier, P., 2014. Large scale bleaching of red beds related to upward migration of hydrocarbons: Los Chihuidos High, Neuquén Basin. Argentina. J. Sed. Res. 84, 373–393. https://doi.org/10.2110/jsr.2014.31.
Rainoldi, A.L., Franchini, M., Beaufort, D., Mozley, P., Giusiano, A., Cesaretti, N., Patrier, P., Pons, M.J., 2015. Mineral reaction associated with hydrocarbons paleomigrations in the Huincul High, Neuquén Basin, Argentina. Geol Soc Amer Bull 127, 1711–1729. https://doi.org/10.1130/B31201.1.
Rainoldi, A.L., Franchini, M., Boyce, A.J., Giusiano, A., Cesaretti, N.N., Pons, J., Ríos, J., 2019. Stable isotope and fluid inclusion study of sediment-hosted stratiform copper deposits from the Neuquén Basin. Argentina. Miner. Deposita 54, 415–436. https://doi.org/10.1007/s00126-018-0815-3.
Ramos, V.A., Barbieri, M., 1989. El volcanismo Cenozoico de Huantrairco: Edad y relaciones isotópicas iniciales, provincia del Neuquén: Rev. Asoc. Geol. Arg. 53, 210–223 (in Spanish).
Salmien, R. (Chief-editor), Batista, M.J., Bidovec, M., Demetriades, A., De Vivo, B., De Vos, W., Duris, M.,Gilucis, A., Gregorauskiene, V., Halamic, J., Heitzmann, P., Lima, A., Jordan, G., Klaver, G., Klein, P., Lis, J., Locutura, J., Marsina, K., Mazreku, A., O'Connor, P.J., Olsson, S.Å., Ottesen, R.T., Petersell, V., Plant, J.A., Reeder, S., Salpeteur, I., Sandström, H., Siewers, U., Steenfelt, A., Tarvainen, T., 2005. Geochemical Atlas of Europe, Part 1 Background Information, Methodology and Maps. Geological Survey of Finland, 526 pp.
Schmid, S., Taylor, W.R., Jordan, D., 2020. The Bigrlyi tabular sandstone-hosted uranium-vanadium deposit, Ngalia Basin. Central Australia. Minerals 10, 896.

Spalletti, L.A., Schwarz, E., Veiga, G.D., 2014. Geoquímica inorgánica como indicador de procedencia y ambiente sedimentario en sucesiones de lutitas negras: los depósitos transgresivos titonianos Formación Vaca Muerta) de la Cuenca Neuquina, Argentina. Andean Geol. 41, 401-435 (in Spanish with English abstract). http://dx.doi.org/10.5027/andgeoV41n2-a07.

Surdam, R.C., Crossey, L.J., Hagen, E.S., Heasler, H.P., 1989. Organic–inorganic interactions and sandstone diagenesis. AAPG Bull. 73, 1–32.

Surdam, R.C., Boese, S.W., Crossey, L.J., 1984. The chemistry of secondary porosity. In: McDonald, O., Surdam, R. (Eds.), Clastic diagenesis: AAPG Memoir 37, pp. 127-149.

Testi, A., Giusiano, A., 2020. Mineralización de V-Cu-U en un frente redox en el Grupo Neuquén, Prospecto Campesino Norte. Cuenca Neuquina, Neuquén, Argentina, in: Proc. XII Congreso Geológico Argentino de Geología Económica, Argentina, 63-68 (in Spanish).

Thyne, G., Boudreau, B.P., Ramm, M., Elin Midtbø, R., 2001. Simulation of potassium feldspar dissolution and illitization in the Statfjord Formation. North Sea. AAPG Bull. 85, 621–635.

Tunik, M., Pons, J., Pimentel, M., Ramos, V.A., 2008. Procedencia de los depósitos sinorogénicos del Grupo Neuquén (cuenca neuquina del sur de Mendoza y Neuquén), in: Proc. XVII Congreso Geológico Argentino, Argentina, 1310-1311 (in Spanish).

Turkekian, K.K., Wedepohl, K.H., 1961. Distribution of the elements in some major units of the Earth's crust. Geol. Soc. Am. Bull. 72, 175–192.

Velde, B., 1985. Clay Minerals: A Physico-Chemical Explanation of Their Occurrence: Amsterdam, Elsevier, Developments in Sedimentology 40, 427 pp.

Vergani, G.D., Tankard, A.J., Belotti, H.J., Welsink, H.J., 1995. Tectonic Evolution and Paleogeography of the Neuquén Basin, Argentina. In: Tankard, A.J., Suárez, S.R., Welsink, H.J. (Eds.), Petroleum basins of South America: AAPG Memoir 62, pp. 383-402.

Vottero, A., González, J.M., 2002. Los reservorios de la Formación Mulichinco. In: Schiuma, M., Hinterwimmer, G., Vergani, G. (Eds.), Rocas reservorio de las cuencas productivas De La Argentina. V Congreso de Exploración y Desarrollo de Hidrocarburos, Mar del Plata, Argentina, pp. 383–400 (in Spanish).

Wanty, R.B., 1986. Geochemistry of Vanadium in an Epigenetic Sandstone-Hosted Vanadium-Uranium Deposit, Henry Basin Utah. Colorado School of Mines, Golden, Colo. Ph.D. thesis.

Wanty, R.B., Goldhaber, M.B., 1992. Thermodynamics and kinetics of reactions involving vanadium in natural systems: accumulation of vanadium in sedimentary rocks. Geochim. Cosmochim. Acta 56, 1471–1483.

Whitney, G., Northrop, H.R., 1986. Vanadium chlorite from a sandstone-hosted vanadium-uranium deposit, Henry Basin. Utah. Clay Clay Mineral. 34, 488–495.

Wilkinson, M., Haszeldine, R.S., Milliken, K., 2003. Cross-formational flux of aluminium and potassium in Gulf Coast (USA) sediments. In: Worden, R.H., Morad, S. (Eds.), Clay Mineral Cements in Sandstones. Int. Assoc. Sedimentol. Special Publication 34, pp.147-160.

Zamora Valcarce, G., Zapata, T., Ramos, V.A., Rodríguez, F., Bernardo, L.M., 2009. Evolución tectónica del frente Andino en Neuquén: Rev. Asoc. Geol. Arg. 65, 192–203 (in Spanish with English abstract).

Zavala, C., Martínez Lampe, J.M., Fernández, M., Di Meglio, M., Arcuri, M., 2008. El diacronismo entre las Formaciones Tordillo y Quebrada del Sapo (Kimeridgiano) en el sector sur de la cuenca neuquina. Rev. Asoc. Geol. Arg. 63, 754–765 (in Spanish with English abstract).

Zientek, M.L., Wintzer, N.E., Hayes, T.S., Parks, H.L., Briggs, D.A., Causey, J.D., Hatch, S. A., Jenkins, M.C., Williams, D.J., 2015. Qualitative assessment of selected areas of the world for undiscovered sediment-hosted stratabound copper deposits. U.S. Geological Survey Scientific Investigations Report 2010–5090–Y.